

Effect of shunted piezoelectric control for tuning piezoelectric power harvesting system responses – Analytical techniques

M F Lumentut* and I M Howard

Laboratory for Dynamic Systems of Smart Structure and Vibration,
Department of Mechanical Engineering,
Curtin University, Australia

Abstract. This paper presents new analytical modelling of shunt circuit control responses for tuning electromechanical piezoelectric vibration power harvesting structures with proof mass offset. For this combination, the dynamic closed-form boundary value equations reduced from strong form variational principles were developed using the extended Hamiltonian principle to formulate the new coupled orthonormalised electromechanical power harvesting equations showing combinations of the mechanical system (dynamical behaviour of piezoelectric structure), electromechanical system (electrical piezoelectric response) and electrical system (tuning and harvesting circuits). The reduced equations can be further formulated to give the complete forms of new electromechanical multi-mode FRFs and time waveform of the standard AC-DC circuit interface. The proposed technique can demonstrate self-adaptive harvesting response capabilities for tuning the frequency band and the power amplitude of the harvesting devices. The self-adaptive tuning strategies are demonstrated by modelling the shunt circuit behaviour of the piezoelectric control layer in order to optimise the harvesting piezoelectric layer during operation under input base excitation. In such situations, with proper tuning parameters the system performance can be substantially improved. Moreover, the validation of the closed-form technique is also provided by developing the Ritz method-based weak form analytical approach giving similar results. Finally, the parametric analytical studies have been explored to identify direct and relevant contributions for vibration power harvesting behaviours.

Keyword: analytical closed form and weak form, frequency response, piezoelectric, power harvesting, shunt control, signal analysis, time waveform, vibration.

1. Introduction

The vast majority of autonomous piezoelectric structures in the various engineering applications encompass shunt control and energy harvesting systems. These two research works are obviously investigated separately in many previous publications. In one hand, piezoelectric shunt control also known as passive circuit control is aimed at the use of vibration suppression in smart structures. On the other hand, electrical power capture of piezoelectric structures using input from the surrounding vibration has been an attractive field in the application of self-powered smart wireless sensor systems. Interestingly, both research areas can provide similar technical insight giving complementary benefit for vibration power harvesting devices since the idea is for matching the resonance of the device to

the dominant frequency of the ambient vibration source and for tuning the frequency band to maximise the system amplitude. Many research efforts have been devoted to improving the piezoelectric energy harvesters using different interface circuit systems in order to optimise their system performance levels. Some of them have been devoted to developing various analytical techniques of the standard cantilever laminated piezoelectric power harvesting devices. Starting with the electrical equivalent system, the simplified lumped parameter models with resistive impedance [1-2] and AC-DC power generation [3] followed by the synchronized switching harvesting on an inductor (SSHI) in the harvesting circuit [4-5] and synchronized charge extraction (SCE) technique [6] have been developed to increase power output in many different case studies. Due to increasing demand of accuracy, analytical techniques of the typical laminated piezoelectric beam structures connected with resistive shunt circuit have used different system approaches such as Rayleigh-Ritz method [7-10], distributed parameter system [11], electromechanical weak-form techniques [12-13], closed form techniques [14], and assumed-mode method [15], transfer matrix method [16] and analytical modal analysis method with AC-DC rectification [17]. For effective and alternative approaches, the numerical techniques using ANSYS software [18-20] have been developed. Then, continuing numerical works have presented the formulations of finite element models of the distributed system [21] and the new electromechanical finite element analysis of the laminated structure with tip mass offset [22].

The recent energy harvesting techniques have also been broadened into frequency tuning systems. For the mechanical tuning system, starting with the use of a tip mass on the end of the smart structure, a shift in frequency from high to low value has become a common practice, especially when the piezoelectric structure is relative small [1, 7, 11-13]. Another [23] has used a movable mass to reach the particular desired tuning frequency range. Then, further works have been developed into particular multimodal power harvesting concepts using one or more auxiliary beams connected to the main piezoelectric beam [24-27]. Moreover, another recent alternative way for widening multifrequency bandwidth of energy harvesting systems involves the use of multiple piezoelectric beams with various electrical connection patterns with specific focus on the mathematical techniques [28-30]. The development has included the specific theoretical works of parallel and series piezoelectric connections with circuit interface using the impedance approach [31] and the SSHI system [32-33]. For the electrical tuning system, it was found that so far only a few published research works have discussed the adaptive resonance smart structure by tuning the electrical piezoelectric element either by using a segmented electrode or layer system such that the power harvesting from another piezoelectric element can be extracted. This also includes the tuning and harvesting circuit network system that are connected together for the self-tuning and power generation system [34-35], while others [36-37] used a separate circuit system for the tuning circuit with capacitors and resistive load for harvesting power.

Other applications of the piezoelectric transducer have also been developed for the shunt control circuit of the smart structure. Although the piezoelectric shunt control system is used to suppress the vibration of the smart structure, the technical study, however provides direct fundamental concepts for developing energy harvesting systems as indicated in the previous examples using either the resistive shunt circuit or switch circuit system or even the electrical tuning system. Moreover, the benefit can also be found in devising self-adaptive energy harvesting systems, capable of having a continuously shifting frequency response band and periodical tuning in the time-power domain as proposed in this paper. Original contribution of shunt circuit control was first introduced using LC circuits [38]. The characteristics of the piezoelectric shunt control mainly consists of the RL circuit (along with inherent piezoelectric capacitance) acting as the passive electrical network for tuning the amplitude response of the smart structure [39-43]. Since targeting the control system to a certain resonance frequency of the system requires large inductance up to thousands of Henries [44], the synthetic inductor or gyrator [45-46] must be utilised. The original contribution of the gyrator itself was first introduced using impedance analysis [47]. Furthermore, the multimode shunt circuit with the RLC branches using numerous tuning techniques for the piezoelectric structures [48-55] was also developed for the multimode suppression of the system.

In the aforementioned works, the two independent technical developments of the piezoelectric systems have significantly contributed to the power harvesting and shunt control smart structure applications. The electrical tuning system raises the issue underpinning the crucial techniques using the electrical network system as shunt circuit control and power harvesting circuit system connected to the piezoelectric elements. Interestingly, as discovered with technical limitations of the previous power harvesting research works, this research work shows that the combination of the shunt circuit control and power harvesting system using proper techniques can demonstrate self-adaptive harvesting response capabilities. In this paper, novel analytical techniques of the coupled system of shunted control and electromechanical piezoelectric power harvester structure with proof mass offset have been developed using the extended Hamiltonian principle for deriving the dynamical closed-form boundary value equations. At this stage, there are no other publications addressing the development of the proposed new analytical techniques with the combinations of the tuning and harvesting circuits, mechanical system (elasticity with mechanical stress and dynamic motions), and electromechanical system (electrical displacement, electrical stress and electric-polarity field). As a result of these combinations, the normalised closed-form electromechanical transverse dynamic equations were reduced to formulate the complete forms of electromechanical multi-mode FRFs. Since the main focus is to develop the closed-form technique, the weak form analytical approach based on the Ritz method, has also been briefly developed for the use of validation showing similar results to that of the closed-form solution. Parametric case studies have been explored for identifying

the most feasible adaptive tuning frequency, amplitude and time waveform power harvesting system responses.

2. Constitutive electromechanical equations

In the robust coupled system as shown in Fig. 1a, the smart structure with proof mass offset under base excitation consists of three layers (tuning piezoelectric, substructure and harvesting piezoelectric), connected with two separated circuit systems. On the lower layer, passive shunt circuit control using RL paralleled with C circuit is used for tuning the system response of the structure. For the upper layer, the standard harvesting circuit is used for generating power. It is important to note here, if the passive RL shunt circuit and inherent piezoelectric capacitor C_v are in series, implementing shunt circuit resonance will require a very large inductor which is not commercially available because the value of optimal inductance is simply formulated as $L_s = 1/(C_v\omega^2)$ where the resonance of the smart structure is equal to the tuning circuit resonance. For example, by implementing an RL circuit, the smart structure resonance of 45 Hz with inherent piezoelectric capacitor C_v of 18.4 nF requires an inductor of 679.8 H. In this case, the large inductance for the typical shunt circuit can be identified due to the very low inherent piezoelectric capacitance and low resonance of the structure. For practical purposes, implementing an inductor up to thousands of Henries can only be synthesised using the specific inductor or gyrator [44] as has been widely used in the passive shunt circuit of piezoelectric controls [39-43, 48-55]. Moreover, it can also be necessarily tuned in size by adding an external capacitor C in parallel to the shunt circuit RL giving the benefit for self-adaptive tuning system response as shown in Fig. 1b. Details of the mathematical expressions for the simplified piezoelectric tuning circuit of Fig. 1c can be found in the forthcoming section.

Here, the linear piezoelectric beam constitutive equations based on the 3-1 mode of piezoelectric constant operation and 3-3 effect of piezoelectric permittivity can be formulated in terms of stress-electric displacement relation [56-58] as,

$$\begin{aligned} T_1 &= \bar{c}_{11}^E S_1 - e_{31} E_3, \\ D_3 &= e_{31} S_1 + \epsilon_{33}^S E_3, \end{aligned} \quad (1)$$

where the parameters T , S , E and D represent stress, strain, electric field, and electric displacement, respectively. Moreover, coefficients c , e , and ϵ indicate elastic constant, piezoelectric coefficients and permittivity at constant strain, respectively. Note that the notations of the piezoelectric material are written according to the IEEE standards [59]. Also note that Eq. (1) is widely used in many piezoelectric power harvester applications.

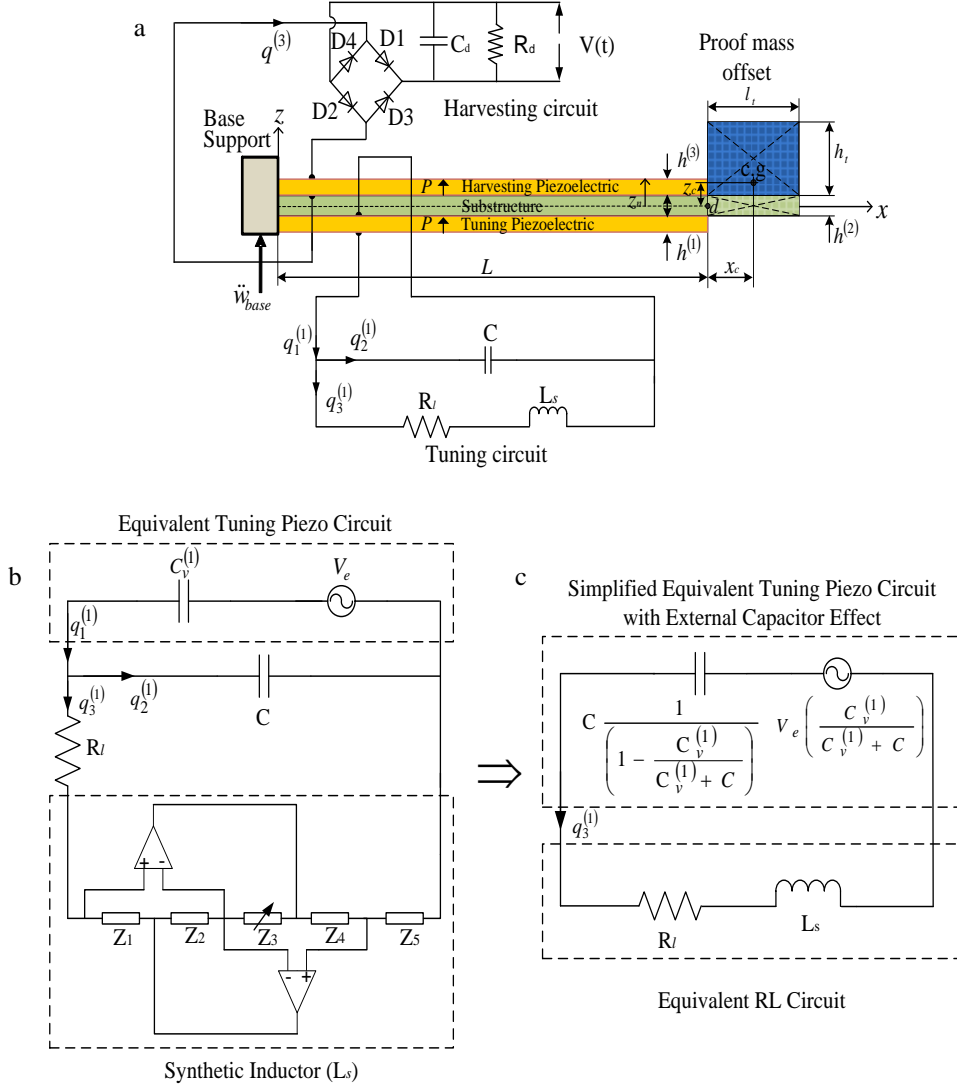


Fig.1. Piezoelectric beam power harvesting with offset proof mass operating under base input excitation: a) physical system, b) tuning circuit for tuning piezoelectric layer, c) simplified tuning circuit for tuning piezoelectric layer.

Since the system as shown in Fig. 1 includes the electrical shunted piezoelectric control system and electrical harvesting piezoelectric system, Eq. (1) can be modified into stress-electric field relations for the tuning piezoelectric material as,

$$\begin{aligned} T_1^{(1)} &= \bar{c}_D^{(1)} S_1^{(1)} - g_{31}^{(1)} D_3^{(1)}, \\ E_3^{(1)} &= -g_{31}^{(1)} S_1^{(1)} + \varepsilon_{33}^{S^{-1}} D_3^{(1)}. \end{aligned} \quad (2)$$

The modified constitutive equations in terms of stress-electric field relations for the harvesting piezoelectric material can be formulated as,

$$\begin{aligned} T_1^{(3)} &= \bar{c}_D^{(3)} S_1^{(3)} - g_{31}^{(3)} D_3^{(3)}, \\ E_3^{(3)} &= -g_{31}^{(3)} S_1^{(3)} + \varepsilon_{33}^{S^{-1}} D_3^{(3)}. \end{aligned} \quad (3)$$

The linear-elastic constitutive relation for the substructure can also be formulated as,

$$T_1^{(2)} = \bar{c}_{11}^{(2)} S_1^{(2)}. \quad (4)$$

Coefficients c_D and g indicate modified elastic constant and modified piezoelectric constant, respectively given in Appendix A. Note that the notations for each layer of the laminated structure in Fig. 1 can be stated in the superscripts, especially for stress T , strain S , elastic stiffness c , density ρ , width b , thickness h , and cross-sectional area A where superscripts 1, 2 and 3 represent the tuning piezoelectric, brass, and harvesting piezoelectric layers, respectively. Here, the strain field for each layer of the beam can be formulated as,

$$S_1(x, t) = -z \frac{\partial^2 w(x, t)}{\partial x^2}, \quad (5)$$

where variable z is the distance from the neutral axis to each layer.

3. Electromechanical closed-form boundary value method

This section deals with development of the new analytical method for the very first time by means of combining the tuning and harvesting circuits, mechanical system (elasticity with mechanical stress and dynamic motions) and electromechanical system (electrical displacement, electrical stress and electric-polarity field). At this stage, two analytical studies using closed-form boundary value method reduced from strong form of variational principle are provided here. First, the piezoelectric energy harvesting coupled with tuning circuit and standard resistive circuit (non-rectifier) was formulated. Second, the piezoelectric energy harvesting coupled with tuning circuit and standard AC-DC interface (rectifier with capacitor and resistor) as shown in Fig. 1 was formulated.

3.1. Coupled System of Electrical Shunted Circuit and Standard Harvesting AC Circuit.

This section derives the key equations of the coupled tuning and standard resistive circuit systems for piezoelectric energy harvesters using the extended Hamiltonian principle to give,

$$\left. \int_{t_1}^{t_2} \delta(L_a + W_f) dt = 0 \right\} \begin{array}{l} L_a \in \{KE, PE, WE, WC, WL\} \\ W_f \in \{WF, WR\} \end{array}, \quad (6)$$

$$\text{or} \quad \int_{t_1}^{t_2} (\delta KE - \delta PE - \delta WE + \delta WF - \delta WC + \delta WL + \delta WR) dt = 0. \quad (7)$$

Note that each functional energy term of Eq. (6) can be formulated in Eqs. (8)-(14). The kinetic energy of the structure with the proof mass offset can be reformulated as,

$$KE = \frac{1}{2} \int_0^L \int_{A^{(1)}} \rho^{(1)} \dot{w}(x, t)^2 dA^{(1)} dx + \frac{1}{2} \int_0^L \int_{A^{(2)}} \rho^{(2)} \dot{w}(x, t)^2 dA^{(2)} dx + \frac{1}{2} \int_0^L \int_{A^{(3)}} \rho^{(3)} \dot{w}(x, t)^2 dA^{(3)} dx$$

$$+ \frac{1}{2} I_0^{tip} \dot{w}(L,t)^2 + \frac{1}{2} I_2^{tip} \dot{\theta}(L,t)^2 + I_0^{tip} x_c \dot{w}(L,t) \dot{\theta}(L,t) . \quad (8)$$

Note that since the system is under base excitation in Fig. 1a, the detail of the mathematical equations for the dynamical structure and proof mass offset as shown in the kinetic energy can be found in [22]. They were reduced due to relative displacement $w(x,t)$ defined as the difference between absolute displacement $w_{abs}(x,t)$ and base excitation $w_{base}(t)$. The potential energy or strain energy of the structure can be formulated as,

$$PE = \frac{1}{2} \int_0^L \int_{A^{(1)}} S_1^{(1)} T_1^{(1)} dA^{(1)} dx + \frac{1}{2} \int_0^L \int_{A^{(2)}} S_1^{(2)} T_1^{(2)} dA^{(2)} dx + \frac{1}{2} \int_0^L \int_{A^{(3)}} S_1^{(3)} T_1^{(3)} dA^{(3)} dx . \quad (9)$$

The electrical energy term for the piezoelectric elements can be formulated to give,

$$WE = \frac{1}{2} \int_0^L \int_{A^{(1)}} E_3^{(1)} D_3^{(1)} dA^{(1)} dx + \frac{1}{2} \int_0^L \int_{A^{(3)}} E_3^{(3)} D_3^{(3)} dA^{(3)} dx . \quad (10)$$

The magnetic co-energy of the inductor in terms of the tuning circuit can be formulated as,

$$WL = \frac{1}{2} L_s \dot{q}_3^{(1)}(t)^2 . \quad (11)$$

where the synthetic inductance value from Fig. 1b can be reduced from the equivalent impedance analysis, $Z_{in} = (Z_1 Z_3 Z_5) / (Z_2 Z_4)$ by allowing the relations $Z_1 = R_1$, $Z_2 = R_2$, $Z_3 = R_3$, $Z_5 = R_5$, and $Z_4 = 1/(j\omega C_s)$ to give $Z_{in} = j\omega L_s$ [44-46]. Therefore, the synthetic inductance value can be formulated as,

$$L_s = \frac{R_1 R_3 R_5 C_s}{R_2} . \quad (12)$$

The electrical energy of the capacitor in terms of the tuning circuit can be formulated as,

$$WC = \frac{1}{2C} q_2^{(1)}(t)^2 . \quad (13)$$

The non-conservative work on the system due to the input base excitation can be stated as,

$$WF = - \int_0^L \int_{A^{(1)}} \rho^{(1)} w(x,t) dA^{(1)} dx \ddot{w}_{base}(t) - \int_0^L \int_{A^{(2)}} \rho^{(2)} w(x,t) dA^{(2)} dx \ddot{w}_{base}(t) - \int_0^L \int_{A^{(3)}} \rho^{(3)} w(x,t) dA^{(3)} dx \ddot{w}_{base}(t) \\ - I_0^{tip} x_c \dot{\theta}(L,t) \ddot{w}_{base}(t) - I_0^{tip} w(L,t) \ddot{w}_{base}(t) . \quad (14)$$

Contribution of the dynamical beam structure and proof mass offset as shown in non-conservative work can be found in [22]. The electrical work dissipated by resistors can be stated as,

$$\delta WR = -R_l \dot{q}_3^{(1)}(t) \delta q_3^{(1)}(t) - R_d \dot{q}^{(3)}(t) \delta q^{(3)}(t) . \quad (15)$$

The functional forms L_a and W_f from Hamiltonian's principle can be seen as the continuous differentiable functions of virtual displacement, electric displacement and charge for the whole system that can be stated as,

$$L_a = L_a \left(\dot{w}(x,t), \dot{w}(L,t), \frac{\partial \dot{w}(L,t)}{\partial x}, \frac{\partial^2 w(x,t)}{\partial x^2}, D_3^{(1)}(z,t), D_3^{(3)}(z,t), q_2^{(1)}(t), \dot{q}_3^{(1)}(t) \right), \quad (16)$$

$$W_f = W_f \left(w(x,t), \frac{\partial w(L,t)}{\partial x}, w(L,t), q_3^{(1)}(t), q^{(3)}(t) \right). \quad (17)$$

Equations (16) and (17) can be further formulated using total differential equations as,

$$\begin{aligned} \delta L_a = & \frac{\partial L_a}{\partial \dot{w}(x,t)} \delta \dot{w}(x,t) + \frac{\partial L_a}{\partial \dot{w}(L,t)} \delta \dot{w}(L,t) + \frac{\partial L_a}{\partial \left(\frac{\partial \dot{w}}{\partial x}(L,t) \right)} \delta \left(\frac{\partial \dot{w}}{\partial x}(L,t) \right) + \frac{\partial L_a}{\partial \left(\frac{\partial^2 w(x,t)}{\partial x^2} \right)} \delta \left(\frac{\partial^2 w(x,t)}{\partial x^2} \right) \\ & + \frac{\partial L_a}{\partial D_3^{(1)}(z,t)} \delta D_3^{(1)}(z,t) + \frac{\partial L_a}{\partial D_3^{(3)}(z,t)} \delta D_3^{(3)}(z,t) + \frac{\partial L_a}{\partial q_2^{(1)}(t)} \delta q_2^{(1)}(t) + \frac{\partial L_a}{\partial \dot{q}_3^{(1)}(t)} \delta \dot{q}_3^{(1)}(t), \end{aligned} \quad (18)$$

$$\delta W_f = \frac{\partial W_f}{\partial w(x,t)} \delta w(x,t) + \frac{\partial W_f}{\partial \left(\frac{\partial w}{\partial x}(L,t) \right)} \delta \left(\frac{\partial w}{\partial x}(L,t) \right) + \frac{\partial W_f}{\partial w(L,t)} \delta w(L,t) + \frac{\partial W_f}{\partial q_3^{(1)}(t)} \delta q_3^{(1)}(t) + \frac{\partial W_f}{\partial q^{(3)}(t)} \delta q^{(3)}(t). \quad (19)$$

Corresponding with Eqs. (8)-(15) and (18)-(19), Eq. (7) can be further formulated using integro-differential equations and the variational principle to give the dynamical closed-form boundary value equation reduced from the strong form method as,

$$\begin{aligned} & \int_{t_1}^{t_2} \left[\int_0^L \left\{ -I_0 \ddot{w}(x,t) - I_0 \ddot{w}_{base}(t) - C_t \frac{\partial^2}{\partial x^2} \left(\frac{\partial^2 w(x,t)}{\partial x^2} \right) \right\} \delta w(x,t) dx \right. \\ & - \left\{ x_c I_0^{tip} \frac{\partial \ddot{w}(L,t)}{\partial x} + I_0^{tip} \ddot{w}(L,t) + I_0^{tip} \ddot{w}_{base} \right\} \delta w(L,t) + C_t \frac{\partial}{\partial x} \left(\frac{\partial^2 w(x,t)}{\partial x^2} \right) \delta w(x,t) \Big|_0^L \\ & - \left\{ I_2^{tip} \frac{\partial \ddot{w}(L,t)}{\partial x} + x_c I_0^{(tip)} \ddot{w}_{base} + x_c I_0^{tip} \ddot{w}(L,t) \right\} \delta \frac{\partial w(L,t)}{\partial x} - \eta^{(1)} q_1^{(1)} \delta \frac{\partial w(x,t)}{\partial x} \Big|_0^L \\ & - \eta^{(3)} q^{(3)}(t) \delta \frac{\partial w(x,t)}{\partial x} \Big|_0^L - C_t \frac{\partial^2 w(x,t)}{\partial x^2} \delta \frac{\partial w(x,t)}{\partial x} \Big|_0^L - \left\{ \int_0^L \eta^{(1)} \frac{\partial^2 w(x,t)}{\partial x^2} dx + \frac{q_1^{(1)}(t)}{C_v^{(1)}} \right\} \delta q_1^{(1)}(t) \\ & - \left\{ \int_0^L \eta^{(3)} \frac{\partial^2 w(x,t)}{\partial x^2} dx + \frac{q^{(3)}(t)}{C_v^{(3)}} \right\} \delta q^{(3)}(t) - \left(L_s \ddot{q}_3^{(1)}(t) + R_l \dot{q}_3^{(1)}(t) \right) \delta q_3^{(1)}(t) \\ & \left. - \frac{q_2^{(1)}(t) \delta q_2^{(1)}(t)}{C} - R_d \dot{q}^{(3)}(t) \delta q^{(3)}(t) \right] dt = 0. \end{aligned} \quad (20)$$

Note that parameter D_3 for two piezoelectric layers implied in Eq. (16) has been modified in Eq. (20) using $D_3^{(1)} = q_1^{(1)}/b^{(1)}L$ and $D_3^{(3)} = q^{(3)}/b^{(3)}L$. Each coefficient in Eq. (20) can be found in Appendices B, C, and D. Also note that the zeroth mass moment of inertia of all layers was given as

$I_0 = \sum_{i=1}^m \rho^{(i)} b^{(i)} h^{(i)}$ where parameter b is the width of the interlayer and term m is number of layers.

Moreover, other parameters of zeroth and second mass moment of inertias of tip mass offset I_0^{tip} and I_2^{tip} can be found in [22]. However, the neutral axis z_n used in the geometry calculation of the tip mass must be based on Appendix C. Applying KCL for the tuning circuit in Fig. 1 gives the electric charge equation as,

$$q_1^{(1)} = q_2^{(1)} + q_3^{(1)}. \quad (21)$$

As shown, variable $q_2^{(1)}$ in Eq. (20) can be eliminated in the forthcoming reduced equations for simplicity using the relation as,

$$\frac{q_2^{(1)}(t)}{C} \delta q_2^{(1)}(t) = \frac{q_1^{(1)}(t)}{C} \delta q_1^{(1)}(t) - \frac{q_3^{(1)}(t)}{C} \delta q_1^{(1)}(t) - \frac{q_1^{(1)}(t)}{C} \delta q_3^{(1)}(t) + \frac{q_3^{(1)}(t)}{C} \delta q_3^{(1)}(t). \quad (22)$$

After applying duBois-Reymond's theorem for each virtual displacement field, the first constitutive electromechanical dynamic equation reduced from Eq. (20) can be formulated as,

$$\delta w(x,t): I_0 \ddot{w}(x,t) + I_0 \ddot{w}_{base}(t) + C_t \frac{\partial^2}{\partial x^2} \left(\frac{\partial^2 w(x,t)}{\partial x^2} \right) = 0. \quad (23)$$

The second, third and fourth constitutive electromechanical dynamic equations related to the coupled tuning and harvesting circuits of piezoelectric structure can be formulated as,

$$\begin{aligned} \delta q_1^{(1)}(t) : \int_0^L \eta^{(1)} \frac{\partial^2 w(x,t)}{\partial x^2} dx + \left(\frac{1}{C_v^{(1)}} + \frac{1}{C} \right) q_1^{(1)}(t) - \frac{q_3^{(1)}(t)}{C} &= 0, \\ \delta q_3^{(1)}(t) : L_s \ddot{q}_3^{(1)}(t) + R_l \dot{q}_3^{(1)}(t) + \frac{q_3^{(1)}(t)}{C} - \frac{q_1^{(1)}(t)}{C} &= 0, \\ \delta q^{(3)}(t) : \int_0^L \eta^{(3)} \frac{\partial^2 w(x,t)}{\partial x^2} dx + \frac{q^{(3)}(t)}{C_v^{(3)}} + R_d \dot{q}^{(3)}(t) &= 0. \end{aligned} \quad (24)$$

The boundary conditions can be formulated as,

$$\begin{aligned} w(0,t) = 0 \quad , \quad \frac{\partial w(0,t)}{\partial x} &= 0, \\ \delta w(L,t) : x_c I_0^{tip} \frac{\partial \ddot{w}(L,t)}{\partial x} + I_0^{tip} \ddot{w}(L,t) + I_0^{tip} \ddot{w}_{base} - C_t \frac{\partial}{\partial x} \left(\frac{\partial^2 w(L,t)}{\partial x^2} \right) &= 0, \\ \delta \frac{\partial w(L,t)}{\partial x} : x_c I_0^{tip} \ddot{w}_{base} + x_c I_0^{tip} \ddot{w}(L,t) + I_2^{tip} \frac{\partial \ddot{w}(L,t)}{\partial x} + C_t \frac{\partial^2 w(L,t)}{\partial x^2} + \eta^{(1)} q_1^{(1)}(t) + \eta^{(3)} q^{(3)}(t) &= 0. \end{aligned} \quad (25)$$

The solution form of Eqs.(23)-(25) can be formulated using mode superposition depending on the normalised mode shapes and generalised time dependent coordinates to give,

$$w(x,t) = \sum_{r=1}^{\infty} \hat{W}_r(x) w_r(t). \quad (26)$$

The normalised mode shape can be proved as shown in Appendix E. Eq. (23) can be reformulated by substituting Eq. (26) and then multiplying with $\hat{W}_q(x)$ and integrating with respect to x to give,

$$\int_0^L I_0 \hat{W}_r(x) \hat{W}_q(x) \ddot{w}_r(t) dx + \int_0^L C_t \frac{d^2}{dx^2} \left(\frac{d^2 \hat{W}_r(x)}{dx^2} \right) \hat{W}_q(x) w_r(t) dx + \int_0^L I_0 \hat{W}_q(x) \ddot{w}_{base}(t) dx = 0. \quad (27)$$

Eqs. (24a) and (24c) can also be further formulated by applying Eq. (26) to give,

$$\begin{aligned} \sum_{r=10}^{\infty} \int_0^L \eta^{(1)} \frac{d^2 \hat{W}_r(x)}{dx^2} dx w_r(t) + \left(\frac{1}{C_v^{(1)}} + \frac{1}{C} \right) q_1^{(1)}(t) - \frac{q_3^{(1)}(t)}{C} &= 0, \\ \sum_{r=10}^{\infty} \int_0^L \eta^{(3)} \frac{d^2 \hat{W}_r(x)}{dx^2} dx w_r(t) + \frac{q^{(3)}(t)}{C_v^{(3)}} + R_d \dot{q}^{(3)}(t) &= 0. \end{aligned} \quad (28)$$

Substituting Eq. (28a) into Eq.(24b) gives,

$$\sum_{r=10}^{\infty} \int_0^L \frac{\eta^{(1)} C_v^{(1)}}{C_v^{(1)} + C} \frac{d^2 \hat{W}_r(x)}{dx^2} dx w_r(t) + \frac{1}{C} \left(1 - \frac{C_v^{(1)}}{C_v^{(1)} + C} \right) q_3^{(1)}(t) + L_s \dot{q}_3^{(1)}(t) + R_l \dot{q}_3^{(1)}(t) = 0. \quad (29)$$

Moreover, applying Eq. (26) into the boundary conditions from Eq. (25) gives,

$$\begin{aligned} \hat{W}_r(0) = 0 \quad , \quad \frac{d\hat{W}_r(0)}{dx} = 0 \quad , \\ x_c I_0^{tip} \frac{d\hat{W}(L)}{dx} \ddot{w}(t) + I_0^{tip} \hat{W}_r(L) \ddot{w}(t) + I_0^{tip} \ddot{w}_{base} - C_t \frac{d}{dx} \left(\frac{d^2 \hat{W}(L)}{dx^2} \right) w_r(t) = 0, \\ x_c I_0^{tip} \ddot{w}_{base}(t) + x_c I_0^{tip} \hat{W}(L) \ddot{w}(t) + I_2^{tip} \frac{d\hat{W}(L)}{dx} \ddot{w}(t) + C_t \frac{d^2 \hat{W}(L)}{dx^2} w(t) \\ + \eta^{(1)} q_1^{(1)}(t) + \eta^{(3)} q^{(3)}(t) = 0. \end{aligned} \quad (30)$$

The second term of (27) needs to be further manipulated using partial integration and orthogonality relations and then applying the boundary conditions from (30a) and multiplying by $w_r(t)$ to give,

$$\begin{aligned} \int_0^L C_t \frac{d^2}{dx^2} \left(\frac{d^2 \hat{W}_r(x)}{dx^2} \right) \hat{W}_q(x) w_r(t) dx = C_t \frac{d}{dx} \left(\frac{d^2 \hat{W}_r(L)}{dx^2} \right) \hat{W}_q(L) w_r(t) \\ - C_t \frac{d^2 \hat{W}_r(L)}{dx^2} \frac{d\hat{W}_q(L)}{dx} w_r(t) + \int_0^L C_t \frac{d^2 \hat{W}_r(x)}{dx^2} \frac{d^2 \hat{W}_q(x)}{dx^2} w_r(t) dx. \end{aligned} \quad (31)$$

Substituting Eqs. (30b)-(30c) into (31) gives,

$$\int_0^L C_t \frac{d^2}{dx^2} \left(\frac{d^2 \hat{W}_r(x)}{dx^2} \right) \hat{W}_q(x) w_r(t) dx = I_0^{tip} \hat{W}_q(L) \ddot{w}_{base} + I_0^{tip} \hat{W}_r(L) \hat{W}_q(L) \ddot{w}_r(t)$$

$$\begin{aligned}
& + x_c I_0^{tip} \frac{d\hat{W}_r(L)}{dx} \hat{W}_q(L) \ddot{w}_r + x_c I_0^{tip} \hat{W}_r(L) \frac{d\hat{W}_q(L)}{dx} \ddot{w}_r + x_c I_0^{tip} \frac{d\hat{W}_q(L)}{dx} \ddot{w}_{base}(t) \\
& + I_2^{tip} \frac{d\hat{W}_r(L)}{dx} \frac{d\hat{W}_q(L)}{dx} \ddot{w}_r(t) + \eta^{(1)} \frac{d\hat{W}_q(L)}{dx} q_1^{(1)}(t) + \eta^{(3)} \frac{d\hat{W}_q(L)}{dx} q^{(3)}(t) + \int_0^L C_t \frac{d^2 \hat{W}_r(x)}{dx^2} \frac{d^2 \hat{W}_q(x)}{dx^2} w_r(t) dx. \quad (32)
\end{aligned}$$

Corresponding to (32), Eq. (27) can be reformulated to give,

$$\begin{aligned}
& \int_0^L I_0 \hat{W}_r(x) \hat{W}_q(x) dx \ddot{w}_r(t) + I_0^{tip} \hat{W}_r(L) \hat{W}_q(L) \ddot{w}_r(t) + x_c I_0^{tip} \frac{d\hat{W}_r(L)}{dx} \hat{W}_q(L) \ddot{w}_r(t) \\
& + x_c I_0^{tip} \hat{W}_r(L) \frac{d\hat{W}_q(L)}{dx} \ddot{w}_r(t) + I_2^{tip} \frac{d\hat{W}_r(L)}{dx} \frac{d\hat{W}_q(L)}{dx} \ddot{w}_r(t) + \int_0^L C_t \frac{d^2 \hat{W}_r(x)}{dx^2} \frac{d^2 \hat{W}_q(x)}{dx^2} dx w_r(t) \\
& + \eta^{(1)} \frac{d\hat{W}_q(L)}{dx} q_1^{(1)}(t) + \eta^{(3)} \frac{d\hat{W}_q(L)}{dx} q^{(3)}(t) = - \int_0^L I_0 \hat{W}_q(x) dx \ddot{w}_{base}(t) \\
& - I_0^{tip} \hat{W}_q(L) \ddot{w}_{base}(t) - x_c I_0^{tip} \frac{d\hat{W}_q(L)}{dx} \ddot{w}_{base}(t). \quad (33)
\end{aligned}$$

Considering the orthonormality property of the mechanical dynamic equations from Eq. (33) gives,

$$\begin{aligned}
& \int_0^L I_0 \hat{W}_r(x) \hat{W}_q(x) dx + I_0^{tip} \hat{W}_r(L) \hat{W}_q(L) + x_c I_0^{tip} \frac{d\hat{W}_r(L)}{dx} \hat{W}_q(L) \\
& + x_c I_0^{tip} \hat{W}_r(L) \frac{d\hat{W}_q(L)}{dx} + I_2^{tip} \frac{d\hat{W}_r(L)}{dx} \frac{d\hat{W}_q(L)}{dx} = \delta_{rq}, \\
& \int_0^L C_t \frac{d^2 \hat{W}_r(x)}{dx^2} \frac{d^2 \hat{W}_q(x)}{dx^2} dx = \omega_r^2 \delta_{rq}, \quad (34)
\end{aligned}$$

where δ_{rq} is the Kronecker delta, defined as unity for $q = r$ and zero for $q \neq r$. Note that parameters $\hat{W}_r(x)$ and $\hat{W}_q(x)$ indicate normalised mode shapes. In terms of orthonormality, the Rayleigh mechanical damping can be formulated as,

$$c_{rq} = \gamma \delta_{rq} + \beta \omega_r^2 \delta_{rq} = 2\zeta_r \omega_r \delta_{rq}, \quad (35)$$

where γ and β indicate Rayleigh damping coefficients. Corresponding to Eq. (34), Eq. (33) associated with Eq. (35) can now be reformulated to give the normalised closed-form electromechanical transverse dynamic equations as,

$$\ddot{w}_r(t) + 2\zeta_r \omega_r \dot{w}_r(t) + \omega_r^2 w_r(t) + T_r^{(1)} q_1^{(1)}(t) + T_r^{(3)} q^{(3)}(t) = -Q_r \ddot{w}_{base}(t). \quad (36)$$

Eliminating $q_1^{(1)}(t)$ from Eq. (36) using Eq. (28a) gives,

$$\begin{aligned}
& \ddot{w}_r(t) + 2\zeta_r \omega_r \dot{w}_r(t) + \omega_r^2 w_r(t) - \sum_{r=1}^{\infty} \hat{T}_r^{(1)} T_r^{(1)} \mu C w_r(t) \\
& + T_r^{(1)} \mu q_3^{(1)}(t) + T_r^{(3)} q^{(3)}(t) = -Q_r \ddot{w}_{base}(t). \quad (37)
\end{aligned}$$

Eqs. (28b) and (29) can be further formulated as,

$$\begin{aligned}
L_s \ddot{q}_3^{(1)}(t) + R_l \dot{q}_3^{(1)}(t) + P_C q_3^{(1)}(t) + \sum_{r=1}^{\infty} \hat{T}_r^{(1)} \mu w_r(t) &= 0, \\
R_d \dot{q}^{(3)}(t) + P_V^{(3)} q^{(3)}(t) + \sum_{r=1}^{\infty} \hat{T}_r^{(3)} w_r(t) &= 0.
\end{aligned} \tag{38}$$

It is noted that Eqs. (37) and (38) consist of three new coupled electromechanical power harvesting equations showing the combinations of the mechanical system (dynamical behaviour of piezoelectric structure), electromechanical system (electrical piezoelectric response) and electrical system (tuning and harvesting circuits). These three equations must show dependable relations when formulating electromechanical FRFs as given in the next stage. At this case, since Eqs. (37)-(38) have been normalised, the parameters T_r , \hat{T}_r , P_V , and Q_r can be reduced as,

$$\begin{aligned}
T_r^{(1)} &= \eta^{(1)} \frac{d\hat{W}_r(L)}{dx}, \quad T_r^{(3)} = \eta^{(3)} \frac{d\hat{W}_r(L)}{dx}, \quad \sum_{r=1}^{\infty} \hat{T}_r^{(1)} = \sum_{r=10}^{\infty} \int_0^L \eta^{(1)} \frac{d^2 \hat{W}_r(x)}{dx^2} dx, \\
\sum_{r=1}^{\infty} \hat{T}_r^{(3)} &= \sum_{r=10}^{\infty} \int_0^L \eta^{(3)} \frac{d^2 \hat{W}_r(x)}{dx^2} dx, \quad P_V^{(3)} = \frac{1}{C_V^{(3)}}, \quad P_C = \frac{1}{C} (1 - \mu), \quad \mu = \frac{C_V^{(1)}}{(C_V^{(1)} + C)}, \\
Q_r &= \int_0^L I_0 \hat{W}_r(x) dx + I_0^{tip} \hat{W}_r(L) + x_c I_0^{tip} \frac{d\hat{W}_r(L)}{dx}.
\end{aligned} \tag{39}$$

Note that Eq. (38a) can be expressed into the series equivalent circuit for the tuning piezoelectric system as shown in Fig. 1c where parameter $V_e = \sum_{r=1}^{\infty} \hat{T}_r^{(1)} w_r(t)$ represents the equivalent voltage source generated due to electromechanical piezoelectric coupling and mechanical motion, parameter equivalent capacitor $C/(1 - \mu)$ on the circuit represents $P_C = (1 - \mu)/C$ on the equation and μ is a constant term due to the coupled inherent piezoelectric capacitor and external capacitor. Note that the optimal inductance-based resonance response can be formulated from Eq. (38a) as $L_s = P_C / \omega_r^2$. Again, since the inherent piezoelectric capacitance is a relatively very small value, implementing the shunt resonance frequency whose value is equal to the resonance of the structural system, requires very large inductance. Therefore, the application of synthetic inductance (gyrator) must be employed for the practical purpose. To obtain the multi-mode electromechanical FRFs equations, Eqs. (37)-(38) can be further formulated using Laplace transformation giving the transfer functions which can be reduced into the frequency response relations. After simplification, the multi-mode electromechanical FRFs of the relative transverse displacement equation can be formulated as,

$$\frac{w_r(j\omega)}{-\omega^2 w_{base} e^{j\omega t}} = \frac{\left[\sum_{r=1}^{\infty} \frac{Q_r}{\omega_r^2 - \hat{T}_r^{(1)} T_r^{(1)} \mu C - \omega^2 + j2\zeta_r \omega_r \omega} \right]}{\left[1 - \sum_{r=1}^{\infty} \frac{\hat{T}_r^{(1)} T_r^{(1)} \mu^2}{(\omega_r^2 - \hat{T}_r^{(1)} T_r^{(1)} \mu C - \omega^2 + j2\zeta_r \omega_r \omega) (P_C - L_s \omega^2 + j\omega R_l)} \right] - \left[\sum_{r=1}^{\infty} \frac{\hat{T}_r^{(3)} T_r^{(3)}}{(\omega_r^2 - \hat{T}_r^{(1)} T_r^{(1)} \mu C - \omega^2 + j2\zeta_r \omega_r \omega) (P_V^{(3)} + j\omega R_d)} \right]}. \quad (40)$$

In terms of Eq. (26), Eq. (40) can be modified into functions of position along the structure (x) and frequency domain (ω) to give,

$$\frac{w(x, j\omega)}{-\omega^2 w_{base} e^{j\omega t}} = \frac{\left[\sum_{r=1}^{\infty} \frac{\hat{W}_r Q_r}{\omega_r^2 - \hat{T}_r^{(1)} T_r^{(1)} \mu C - \omega^2 + j2\zeta_r \omega_r \omega} \right]}{\left[1 - \sum_{r=1}^{\infty} \frac{\hat{T}_r^{(1)} T_r^{(1)} \mu^2}{(\omega_r^2 - \hat{T}_r^{(1)} T_r^{(1)} \mu C - \omega^2 + j2\zeta_r \omega_r \omega) (P_C - L_s \omega^2 + j\omega R_l)} \right] - \left[\sum_{r=1}^{\infty} \frac{\hat{T}_r^{(3)} T_r^{(3)}}{(\omega_r^2 - \hat{T}_r^{(1)} T_r^{(1)} \mu C - \omega^2 + j2\zeta_r \omega_r \omega) (P_V^{(3)} + j\omega R_d)} \right]}. \quad (41)$$

The relative transverse displacement FRFs at the end of the proof mass can be formulated as,

$$\frac{w(L + L_{tip}, j\omega)}{-\omega^2 w_{base} e^{j\omega t}} = \frac{\left[\sum_{r=1}^{\infty} \frac{\left(\hat{W}_r(L) + L_{tip} \frac{d\hat{W}_r(x)}{dx} \right) Q_r}{\omega_r^2 - \hat{T}_r^{(1)} T_r^{(1)} \mu C - \omega^2 + j2\zeta_r \omega_r \omega} \right]}{\left[1 - \sum_{r=1}^{\infty} \frac{\hat{T}_r^{(1)} T_r^{(1)} \mu^2}{(\omega_r^2 - \hat{T}_r^{(1)} T_r^{(1)} \mu C - \omega^2 + j2\zeta_r \omega_r \omega) (P_C - L_s \omega^2 + j\omega R_l)} \right] - \left[\sum_{r=1}^{\infty} \frac{\hat{T}_r^{(3)} T_r^{(3)}}{(\omega_r^2 - \hat{T}_r^{(1)} T_r^{(1)} \mu C - \omega^2 + j2\zeta_r \omega_r \omega) (P_V^{(3)} + j\omega R_d)} \right]}. \quad (42)$$

Moreover, the multimode electric charge FRFs at tuning circuit can be formulated as,

$$\frac{q_3^{(1)}(j\omega)}{-\omega^2 w_{base} e^{j\omega t}} = \frac{\left[\sum_{r=1}^{\infty} \frac{Q_r \hat{T}_r^{(1)} \mu}{(\omega_r^2 - \hat{T}_r^{(1)} T_r^{(1)} \mu C - \omega^2 + j2\zeta_r \omega_r \omega) (P_C - L_s \omega^2 + j\omega R_l)} \right]}{\left[1 - \sum_{r=1}^{\infty} \frac{\hat{T}_r^{(1)} T_r^{(1)} \mu^2}{(\omega_r^2 - \hat{T}_r^{(1)} T_r^{(1)} \mu C - \omega^2 + j2\zeta_r \omega_r \omega) (P_C - L_s \omega^2 + j\omega R_l)} \right] - \left[\sum_{r=1}^{\infty} \frac{\hat{T}_r^{(3)} T_r^{(3)}}{(\omega_r^2 - \hat{T}_r^{(1)} T_r^{(1)} \mu C - \omega^2 + j2\zeta_r \omega_r \omega) (P_V^{(3)} + j\omega R_d)} \right]}. \quad (43)$$

The multimode electric charge FRFs of the harvesting circuit can be formulated to give,

$$\frac{q^{(3)}(j\omega)}{-\omega^2 w_{base} e^{j\omega t}} = \frac{\left[\sum_{r=1}^{\infty} \frac{Q_r \hat{T}_r^{(3)}}{(\omega_r^2 - \hat{T}_r^{(1)} T_r^{(1)}) \mu C - \omega^2 + j2\zeta_r \omega_r \omega} (P_V^{(3)} + j\omega R_d) \right]}{\left[1 - \sum_{r=1}^{\infty} \frac{\hat{T}_r^{(1)} T_r^{(1)} \mu^2}{(\omega_r^2 - \hat{T}_r^{(1)} T_r^{(1)}) \mu C - \omega^2 + j2\zeta_r \omega_r \omega} (P_C - L_s \omega^2 + j\omega R_l) \right] - \sum_{r=1}^{\infty} \frac{\hat{T}_r^{(3)} T_r^{(3)}}{(\omega_r^2 - \hat{T}_r^{(1)} T_r^{(1)}) \mu C - \omega^2 + j2\zeta_r \omega_r \omega} (P_V^{(3)} + j\omega R_d) \right]}. \quad (44)$$

Other multimode FRFs relations can also be further formulated by using Eqs. (40)-(44). Here the multi-mode electric current FRFs of the tuning circuit can be formulated as,

$$\frac{i_3^{(1)}(j\omega)}{-\omega^2 w_{base} e^{j\omega t}} = j\omega \frac{q_3^{(1)}(j\omega)}{-\omega^2 w_{base} e^{j\omega t}}. \quad (45)$$

Voltage FRFs across the resistor, inductor and capacitor of the tuning circuit can be formulated respectively as,

$$\begin{aligned} \frac{v_R^{(1)}(j\omega)}{-\omega^2 w_{base} e^{j\omega t}} &= j\omega R_l \frac{q_3^{(1)}(j\omega)}{-\omega^2 w_{base} e^{j\omega t}}, \quad \frac{v_L^{(1)}(j\omega)}{-\omega^2 w_{base} e^{j\omega t}} = -\omega^2 L_s \frac{q_3^{(1)}(j\omega)}{-\omega^2 w_{base} e^{j\omega t}}, \\ \frac{v_C^{(1)}(j\omega)}{-\omega^2 w_{base} e^{j\omega t}} &= \frac{1}{C} \frac{q_2^{(1)}(j\omega)}{-\omega^2 w_{base} e^{j\omega t}}. \end{aligned} \quad (46)$$

Note that parameter $q_2^{(1)}$ in Eq. (46b) can be obtained using Eq. (28a) in terms of Eqs. (21), (40) and (43). Power FRFs across the resistor, inductor and capacitor of the tuning circuit can be formulated respectively as,

$$\begin{aligned} \frac{P_R^{(1)}(j\omega)}{(-\omega^2 w_{base} e^{j\omega t})^2} &= -\omega^2 R_l \frac{q_3^{(1)}(j\omega)^2}{(-\omega^2 w_{base} e^{j\omega t})^2}, \quad \frac{P_L^{(1)}(j\omega)}{(-\omega^2 w_{base} e^{j\omega t})^2} = -j\omega^3 L_s \frac{q_3^{(1)}(j\omega)^2}{(-\omega^2 w_{base} e^{j\omega t})^2}, \\ \frac{P_C^{(1)}(j\omega)}{(-\omega^2 w_{base} e^{j\omega t})^2} &= \frac{j\omega}{C} \frac{q_2^{(1)}(j\omega)^2}{(-\omega^2 w_{base} e^{j\omega t})^2}. \end{aligned} \quad (47)$$

Moreover, the multi-mode electric current FRFs at harvesting circuit can be formulated to give,

$$\frac{i^{(3)}(j\omega)}{-\omega^2 w_{base} e^{j\omega t}} = j\omega \frac{q^{(3)}(j\omega)}{-\omega^2 w_{base} e^{j\omega t}}. \quad (48)$$

Voltage and power FRFs across the resistor of the harvesting circuit can be formulated respectively as,

$$\frac{v_R^{(3)}(j\omega)}{-\omega^2 w_{base} e^{j\omega t}} = j\omega R_d \frac{q^{(3)}(j\omega)}{-\omega^2 w_{base} e^{j\omega t}}, \quad \frac{P_R^{(3)}(j\omega)}{(-\omega^2 w_{base} e^{j\omega t})^2} = -\omega^2 R_d \frac{q^{(3)}(j\omega)^2}{(-\omega^2 w_{base} e^{j\omega t})^2}. \quad (49)$$

Note that the absolute transverse displacement and velocity FRFs can be formulated using Eqs. (41) and (42) to give,

$$\frac{w_{abs}(L+L_{tip}, j\omega)}{-\omega^2 w_{base} e^{j\omega t}} = -\frac{1}{\omega^2} + \frac{w(L+L_{tip}, j\omega)}{-\omega^2 w_{base} e^{j\omega t}}, \quad \frac{\dot{w}_{abs}(L+L_{tip}, j\omega)}{-\omega^2 w_{base} e^{j\omega t}} = \frac{1}{j\omega} + j\omega \frac{w(L+L_{tip}, j\omega)}{-\omega^2 w_{base} e^{j\omega t}}. \quad (50)$$

3.2. Coupled System of Electrical Shunted Circuit and Standard Harvesting AC-DC Interface Circuit.

The operating electrical waveform from the harvesting piezoelectric system was affected by the electrical shunt control of the tuning piezoelectric component as proved in the previous section. During the half-cycle period, the process of the output current of the harvesting piezoelectric through the ideal AC-DC interface circuit can be illustrated in two intervals as shown in Fig 2. For every positive cycle, when diodes D1 and D2 are forward biased and conduct, the output voltage from rectifier v_d is equal to that of harvesting piezoelectric voltage v_p and the current increases for charging. By the time of discharging, diodes D3 and D4 are reverse biased and do not conduct resulting in exponential decay of v_d and no current. During the negative half-cycle, the diodes D3 and D4 will become forward biased and conduct whereas diodes D1 and D2 return to reverse biased.

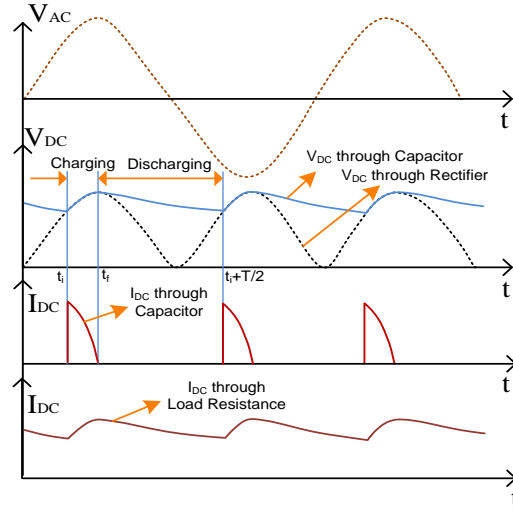


Fig.2. Time waveforms of the standard harvesting circuit

a. Current flowing with interval $t_i < t < t_f$ indicating the charging time over every half-cycle of the frequency.

With the corresponding previous theoretical derivations, the robust coupled system interface of shunt control and harvesting DC rectifier with smoothing RC circuit can be formulated using the previous equations in Eq. (37) with slight modification in Eq. (38b). The following equations of the coupled system response during the period of charging can be formulated as,

$$\ddot{w}_r(t) + 2\zeta_r \omega_r \dot{w}_r(t) + \omega_r^2 w_r(t) - \sum_{r=1}^{\infty} \hat{T}_r^{(1)} T_r^{(1)} \mu C w_r(t) + T_r^{(1)} \mu q_3^{(1)}(t) + T_r^{(3)} q^{(3)}(t) = -Q_r \ddot{w}_{base}(t),$$

$$L_s \ddot{q}_3^{(1)}(t) + R_l \dot{q}_3^{(1)}(t) + P_C q_3^{(1)}(t) + \sum_{r=1}^{\infty} \hat{T}_r^{(1)} \mu w_r(t) = 0,$$

$$v_d + P_V^{(3)} q^{(3)}(t) + \sum_{r=1}^{\infty} \hat{T}_r^{(3)} w_r(t) = 0 \quad . \quad (51)$$

Note that the first term in Eq. (51c) was introduced by replacing the first term from Eq. (38c). This can be obtained by removing the second term in Eq. (15) and introducing the new electrical work done by the harvesting piezoelectric layer $\delta WFr = v_d(t) \delta q^{(3)}(t)$ for the Hamiltonian functional energy in Eq. (7). Differentiating Eq. (51c) with respect to time gives,

$$\dot{v}_d + P_V^{(3)} \dot{q}^{(3)}(t) + \sum_{r=1}^{\infty} \hat{T}_r^{(3)} \dot{w}_r(t) = 0. \quad (52)$$

The equation for the harvesting circuit using the KCL equation can be formulated as,

$$\dot{q}^{(3)}(t) - C_d \dot{v}_d - \frac{v_d}{R_d} = 0. \quad (53)$$

Substituting parameter $q^{(3)}(t)$ from Eq. (51c) into Eq. (51a) and parameter $\dot{q}^{(3)}(t)$ from (52) into Eq. (53), the results of which can be incorporated with Eq. (51b), gives the following state space representation of the multi-mode response system as,

$$\frac{d}{dt} \begin{bmatrix} w_1 \\ w_2 \\ \vdots \\ w_r \\ \dot{w}_1 \\ \dot{w}_2 \\ \vdots \\ \dot{w}_r \\ q_3^{(1)} \\ \dot{q}_3^{(1)} \\ v_d \end{bmatrix} = \begin{bmatrix} \dot{w}_1 \\ \dot{w}_2 \\ \vdots \\ \dot{w}_r \\ -2\zeta_1 \omega_1 \dot{w}_1 - \omega_1^2 w_1 + \hat{T}_1^{(1)} T_1^{(1)} w_1 \mu C - T_1^{(1)} \mu q_3^{(1)}(t) + \frac{\sum_{r=1}^{\infty} \hat{T}_r^{(3)} T_r^{(3)} w_r}{P_V^{(3)}} + \frac{T_1^{(3)} v_d}{P_V^{(3)}} - Q_1 \ddot{w}_{base}(t) \\ -2\zeta_2 \omega_2 \dot{w}_2 - \omega_2^2 w_2 + \hat{T}_2^{(1)} T_2^{(1)} w_2 \mu C - T_2^{(1)} \mu q_3^{(1)}(t) + \frac{\sum_{r=1}^{\infty} \hat{T}_r^{(3)} T_r^{(3)} w_r}{P_V^{(3)}} + \frac{T_2^{(3)} v_d}{P_V^{(3)}} - Q_2 \ddot{w}_{base}(t) \\ \vdots \\ -2\zeta_r \omega_r \dot{w}_r - \omega_r^2 w_r + \hat{T}_r^{(1)} T_r^{(1)} w_r \mu C - T_r^{(1)} \mu q_3^{(1)}(t) + \frac{\sum_{r=1}^{\infty} \hat{T}_r^{(3)} T_r^{(3)} w_r}{P_V^{(3)}} + \frac{T_r^{(3)} v_d}{P_V^{(3)}} - Q_r \ddot{w}_{base}(t) \\ \dot{q}_3^{(1)} \\ \frac{R_l \dot{q}_3^{(1)}}{L_s} - \frac{P_C q_3^{(1)}}{L_s} - \frac{\sum_{r=1}^{\infty} \hat{T}_r^{(1)} \mu w_r}{L_s} \\ - \frac{\sum_{r=1}^{\infty} \hat{T}_r^{(3)} \dot{w}_r}{(P_V^{(3)} C_d + 1)} - \frac{v_d}{\left(R_d C_d + \frac{R_d}{P_V^{(3)}} \right)} \end{bmatrix}. \quad (54)$$

b. Current flowing with interval $t_f < t < t_i + T/2$ indicating the discharging times every half-cycle of the frequency.

For this case, the harvesting circuit can be formulated as,

$$C_d \dot{v}_d + \frac{v_d}{R_d} = 0. \quad (55)$$

The solution form of Eq. (55) can be stated as,

$$v_d(t) = v_d(t_f) \exp\left(\frac{-(t-t_f)}{C_d R_d}\right). \quad (56)$$

Note that the expressions of Eqs. (54) and (56) can be utilized to estimate the current and voltage waveform during the charging and discharging periods.

4. Electromechanical weak form analytical approach

An alternative solution technique can also be formulated using the weak-form reduced from the variational principle corresponding to virtual relative transverse displacement field, harvesting electrical charge and tuning electrical charge. The weak form-based Ritz method [13, 60-61] is further developed here for the tuning piezoelectric power harvesting system. This technique that involves a test function in the essence of the piecewise continuous function for the entire structural domain, requires the straightforward solution that should meet continuity requirements and boundary conditions. In terms of Eqs. (8)-(18), the weak form of Eq. (7) can be formulated as,

$$\begin{aligned} & \int_{t_1}^{t_2} \left[\int_0^L \left\{ I_0 \ddot{w}(x,t) \delta w(x,t) + I_0 \ddot{w}_{base}(t) \delta w(x,t) + C_t \frac{\partial^2 w(x,t)}{\partial x^2} \frac{\partial^2 \delta w(x,t)}{\partial x^2} \right\} dx \right. \\ & + \left\{ x_c I_0^{tip} \frac{\partial \ddot{w}(L,t)}{\partial x} + I_0^{tip} \ddot{w}(L,t) + I_0^{tip} \ddot{w}_{base} \right\} \delta w(L,t) \\ & + \left\{ I_2^{tip} \frac{\partial \ddot{w}(L,t)}{\partial x} + x_c I_0^{(tip)} \ddot{w}_{base} + x_c I_0^{tip} \ddot{w}(L,t) \right\} \delta \frac{\partial w(L,t)}{\partial x} + \int_0^L \left\{ \eta^{(1)} q_1^{(1)} \frac{\partial^2 \delta w(x,t)}{\partial x^2} \right. \\ & + \left. \eta^{(3)} q^{(3)}(t) \frac{\partial^2 \delta w(x,t)}{\partial x^2} \right\} dx + \left\{ \int_0^L \eta^{(1)} \frac{\partial^2 w(x,t)}{\partial x^2} dx + \frac{q_1^{(1)}(t)}{C_v^{(1)}} \right\} \delta q_1^{(1)}(t) \\ & + \left\{ \int_0^L \eta^{(3)} \frac{\partial^2 w(x,t)}{\partial x^2} dx + \frac{q^{(3)}(t)}{C_v^{(3)}} \right\} \delta q^{(3)}(t) + \left(L_s \ddot{q}_3^{(1)}(t) + R_l \dot{q}_3^{(1)}(t) \right) \delta q_3^{(1)}(t) \\ & \left. + \frac{q_2^{(1)}(t) \delta q_2^{(1)}(t)}{C} + R_d \dot{q}^{(3)}(t) \delta q^{(3)}(t) \right] dt = 0 \quad . \quad (57) \end{aligned}$$

Note that each coefficient can be found in Appendices B, C, and D. Moreover, coefficients I_0 , I_0^{tip} and I_2^{tip} have been described after Eq. (20). Eq. (57) still has the variable $q_2^{(1)}$ which can be

eliminated using the relation of Eq. (22) and after simplification the reduced equations can be prescribed using normalised eigenfunction series forms,

$$w(x,t) = \sum_{r=1}^m \hat{W}_r(x) w_r(t) \quad . \quad (58)$$

The first electromechanical dynamic equation represents the coupled tuning-harvesting piezoelectric bimorph under transverse bending form as,

$$\begin{aligned} & \sum_{q=1}^m \left\{ \sum_{r=1}^m \left[\int_0^L I_0 \hat{W}_q(x) \hat{W}_r(x) dx + I_0^{tip} \hat{W}_q(L) \hat{W}_r(L) + x_c I_0^{tip} \frac{d\hat{W}_r(L)}{dx} \hat{W}_q(L) + x_c I_0^{tip} \hat{W}_r(L) \frac{d\hat{W}_q(L)}{dx} \right. \right. \\ & \left. \left. + I_2^{tip} \frac{d\hat{W}_q(L)}{dx} \frac{d\hat{W}_r(L)}{dx} \right) \ddot{w}_r(t) + \int_0^L C_t \frac{d^2 \hat{W}_q(x)}{dx^2} \frac{d^2 \hat{W}_r(x)}{dx^2} w_r(t) dx \right] + \int_0^L \left[\eta^{(1)} \frac{d^2 \hat{W}_q}{dx^2} q_1^{(1)}(t) \right. \\ & \left. + \eta^{(3)} \frac{d^2 \hat{W}_q}{dx^2} q^{(3)}(t) \right] dx + \left(\int_0^L I_0 \hat{W}_q(x) dx + x_c I_0^{tip} \frac{d\hat{W}_q(L)}{dx} + I_0^{tip} \hat{W}_q(L) \right) \ddot{w}_{base}(t) \left. \right\} \delta w_q(t) = 0 \quad .(59) \end{aligned}$$

The second, third and fourth equations represent the electromechanical harvesting piezoelectric, tuning piezoelectric and tuning circuit forms, respectively to give,

$$\begin{aligned} & \left\{ \sum_{r=1}^m \int_0^L \eta^{(3)} \frac{d^2 \hat{W}_r(x,t)}{dx^2} dx + \frac{q^{(3)}(t)}{C_V^{(3)}} + R_d \dot{q}^{(3)}(t) \right\} \delta q^{(3)}(t) = 0 \quad , \\ & \left\{ \sum_{r=1}^m \int_0^L \eta^{(1)} \frac{d^2 \hat{W}_r(x,t)}{dx^2} dx + \left(\frac{1}{C_V^{(1)}} + \frac{1}{C} \right) q_1^{(1)}(t) - \frac{q_3^{(1)}(t)}{C} \right\} \delta q_1^{(1)}(t) = 0, \\ & \left\{ L_s \ddot{q}_3^{(1)}(t) + R_l \dot{q}_3^{(1)}(t) + \frac{q_3^{(1)}(t)}{C} - \frac{q_1^{(1)}(t)}{C} \right\} \delta q_3^{(1)}(t) = 0. \quad (60) \end{aligned}$$

The constitutive equations from Eqs. (59)-(60) can also be reformulated into matrix form by including the mechanical damping coefficients to give,

$$\begin{bmatrix} M_{qr} & 0 & 0 \\ 0 & L_s & 0 \\ 0 & 0 & 0 \end{bmatrix} \begin{Bmatrix} \ddot{w}_r \\ \ddot{q}_3^{(1)} \\ \ddot{q}^{(3)} \end{Bmatrix} + \begin{bmatrix} C_{qr} & 0 & 0 \\ 0 & R_l & 0 \\ 0 & 0 & R_d \end{bmatrix} \begin{Bmatrix} \dot{w}_r \\ \dot{q}_3^{(1)} \\ \dot{q}^{(3)} \end{Bmatrix} + \begin{bmatrix} K_{qr} - P_q^{(1)} P_r^{(1)} \mu C & P_q^{(1)} \mu & P_q^{(3)} \\ P_r^{(1)} \mu & P_C & 0 \\ P_r^{(3)} & 0 & P_V^{(3)} \end{bmatrix} \begin{Bmatrix} w_r \\ q_3^{(1)} \\ q^{(3)} \end{Bmatrix} = \begin{bmatrix} -Q_q & 0 & 0 \\ 0 & 0 & 0 \\ 0 & 0 & 0 \end{bmatrix} \begin{Bmatrix} \ddot{w}_{base} \\ 0 \\ 0 \end{Bmatrix} \quad , (61)$$

where,

$$\begin{aligned} M_{qr} &= \int_0^L I_0 \hat{W}_q(x) \hat{W}_r(x) dx + I_0^{tip} \hat{W}_q(L) \hat{W}_r(L) + x_c I_0^{tip} \frac{d\hat{W}_r(L)}{dx} \hat{W}_q(L) \\ &+ x_c I_0^{tip} \hat{W}_r(L) \frac{d\hat{W}_q(L)}{dx} + I_2^{tip} \frac{d\hat{W}_q(L)}{dx} \frac{d\hat{W}_r(L)}{dx} , \\ K_{qr} &= \int_0^L C_t \frac{d^2 \hat{W}_q(x)}{dx^2} \frac{d^2 \hat{W}_r(x)}{dx^2} dx , \quad P_r^{(1)} = \int_0^L \eta^{(1)} \frac{d^2 \hat{W}_r(x)}{dx^2} dx , \quad P_q^{(1)} = \int_0^L \eta^{(1)} \frac{d^2 \hat{W}_q(x)}{dx^2} dx , \end{aligned}$$

$$P_q^{(3)} = \int_0^L \eta^{(3)} \frac{d^2 \hat{W}_q(x)}{dx^2} dx, P_r^{(3)} = \int_0^L \eta^{(3)} \frac{d^2 \hat{W}_r(x)}{dx^2} dx, P_V^{(3)} = \frac{1}{C_v^{(3)}}, P_C = \frac{1}{C} (1 - \mu),$$

$$\mu = \frac{C_v^{(1)}}{(C_v^{(1)} + C)}, Q_q = \int_0^L I_0 \hat{W}_q(x) dx + I_0^{tip} \hat{W}_q(L) + x_c I_0^{tip} \frac{d \hat{W}_q(L)}{dx}. \quad (62)$$

Eq. (61) represents the normalised differential electromechanical dynamic equation of the coupled tuning-harvesting piezoelectric bimorph beam with tip mass offset under operating input base excitation. Since Eq. (62) involves parameter $\hat{W}_r(\cdot)$ representing the normalised eigenfunction, the normalised mode shapes for the Euler-Bernoulli bimorph beam can be formulated as,

$$\hat{W}_r(x) = \frac{W_r(x)}{\left(\int_0^L I_0 W_r(x)^2 dx + I_0^{tip} W_r(L)^2 + 2x_c I_0^{tip} W_r(L) \frac{dW_r}{dx}(L) + I_2^{tip} \left(\frac{dW_r}{dx}(L) \right)^2 \right)^{1/2}}, r=1,2,\dots, m \quad (63)$$

Parameter $W_r(\cdot)$ can be obtained from the generalized space-dependent Ritz eigenfunctions as,

$$W_r(x) = \sum_{k=1}^m c_{kr} W_k(x) \quad , \quad r=1,2,\dots,m \quad (64)$$

Note that the parameter mode shape $W_k(x)$ can be found in Appendix E and the generalized Ritz coefficient c_{kr} is the eigenvector matrix where each column corresponds to a specific independent eigenvalue. The coefficient can only be proved by replacing Eq. (58) with $w(x,t) = \sum_{r=1}^m c_r W_r(x) e^{i\omega t}$ and rearranging Eq. (61) by considering the characteristic mechanical equation $\sum_{r=1}^m [K_{qr} - \omega^2 M_{qr}] c_r = 0$, $q=1,2,\dots,m$. It should be noted that c_r is called the Ritz coefficient for the mechanical transverse bending form which sometimes refers to the eigenvectors in the mechanical domain. Corresponding to Eqs. (61), the orthonormalisations can now be further proven by using Eq. (63) and applying the orthogonality property of the mechanical dynamic equations for the Euler-Bernoulli bimorph beam as,

$$\int_0^L I_0 \hat{W}_r(x) \hat{W}_q(x) dx + I_0^{tip} \hat{W}_r(L) \hat{W}_q(L) + x_c I_0^{tip} \frac{d \hat{W}_r(L)}{dx} \hat{W}_q(L) + x_c I_0^{tip} \hat{W}_r(L) \frac{d \hat{W}_q(L)}{dx} + I_2^{tip} \frac{d \hat{W}_r(L)}{dx} \frac{d \hat{W}_q(L)}{dx} = \delta_{rq},$$

$$\int_0^L C_t \frac{d^2 \hat{W}_r(x)}{dx^2} \frac{d^2 \hat{W}_q(x)}{dx^2} dx = \omega_r^2 \delta_{rq}, \quad (65)$$

where δ_{rq} is the Kronecker delta, defined as unity for $q = r$ and zero for $q \neq r$. Note that parameters $\hat{W}_r(x)$ and $\hat{W}_q(x)$ indicate normalised mode shapes. Applying the orthonormalisations from Eq. (65) into Eq. (61) gives,

$$\begin{aligned} \ddot{w}_r(t) + 2\zeta_r \omega_r \dot{w}_r(t) + \omega_r^2 w_r(t) - \hat{P}_r^{(1)} P_r^{(1)} \mu C w_r(t) \\ + P_r^{(1)} \mu q_3^{(1)}(t) + P_r^{(3)} q^{(3)}(t) = -Q_r \ddot{w}_{base}(t), \\ L_s \ddot{q}_3^{(1)}(t) + R_l \dot{q}_3^{(1)}(t) + P_C q_3^{(1)}(t) + \hat{P}_r^{(1)} \mu w_r(t) = 0, \\ R_d \dot{q}^{(3)}(t) + P_V^{(3)} q^{(3)}(t) + \sum_{r=1}^{\infty} P_r^{(3)} w_r(t) = 0. \end{aligned} \quad (66)$$

Like the closed-form boundary value equation technique, three coupled equations based on the weak form must also show dependable relations when formulating the electromechanical FRFs and there are similarities between these two techniques with different analytical methods. Moreover, the FRFs provide accurate results as long as the test function-based Ritz eigenfunction is chosen correctly. At this case, since Eq. (66) has been normalised, the parameters P_r and \hat{P}_r can be reduced as,

$$P_r^{(1)} = \int_0^L \eta^{(1)} \frac{d^2 \hat{W}_r(x)}{dx^2} dx, \quad P_r^{(3)} = \int_0^L \eta^{(3)} \frac{d^2 \hat{W}_r(x)}{dx^2} dx, \quad \hat{P}_r^{(1)} = \sum_{r=1}^m P_r^{(1)}, \quad \hat{P}_r^{(3)} = \sum_{r=1}^m P_r^{(3)}. \quad (67)$$

Note that other parameters can be seen in Eq. (62). Laplace transformation can be used to formulate the multi-mode electromechanical FRFs equations giving the transfer functions. Here only one example of the harvesting electrical power FRF is shown across the load resistance after simplification,

$$\frac{P_R^{(3)}(j\omega)}{(-\omega^2 w_{base} e^{j\omega t})^2} = \frac{-\omega^2 R_d \left[\sum_{r=1}^m \frac{Q_r P_r^{(3)}}{(\omega_r^2 - P_r^{(1)2} \mu C - \omega^2 + j2\zeta_r \omega_r \omega)} (P_V^{(3)} + j\omega R_d) \right]}{\left[1 - \sum_{r=1}^m \frac{P_r^{(1)2} \mu^2}{(\omega_r^2 - P_r^{(1)2} \mu C - \omega^2 + j2\zeta_r \omega_r \omega)} (P_C - L_s \omega^2 + j\omega R_l) \right]^2 - \left[\sum_{r=1}^m \frac{P_r^{(3)2}}{(\omega_r^2 - P_r^{(1)2} \mu C - \omega^2 + j2\zeta_r \omega_r \omega)} (P_V^{(3)} + j\omega R_d) \right]^2}. \quad (68)$$

5. Result and discussion

This section discusses parametric case studies of the coupled system of shunted control and electromechanical power harvester of piezoelectric bimorph structure with proof mass offset using velocity and power FRFs and time waveform DC output responses. The studies mainly discuss options to find the most feasible and effective tuning circuit parameters that are applicable for power

harvesting schemes because certain cases of tuning parameters (e.g. optimal tuning circuit parameter) do not give benefit for the power harvesting. The material properties of the piezoelectric bimorph beam are given in Table 1. The piezoelectric material used here was made from PZT PSI-5A4E. The geometrical structures with tip mass offset under input excitation of 1 m/s^2 as shown in Fig. 1 with beam length L and width b with the lower piezoelectric thickness $h^{(1)}$, substructure (brass) thickness $h^{(2)}$ and upper piezoelectric thickness $h^{(3)}$ were set to 60 mm, 6 mm, 0.267 mm, 0.5 mm and 0.508 mm, respectively. The dimensions of the tip mass offset l , h_t and b (width) were set to 15 mm, 10 mm and 6 mm, respectively.

Material properties	Piezoelectric layers	Brass
Young's modulus, \bar{c}_{11} (GPa)	66	105
Density, ρ (kg/m^3)	7800	9000
Piezoelectric constant, d_{31} (pm/V)	-190	-
Permittivity, ϵ_{33}^T (F/m)	$1800 \epsilon_0$	-
permittivity of free space, ϵ_0 (pF/m)	8.854	-

It is important to note here, comparisons between closed form and Ritz methods are used for validations in this paper. Only two validations are given as examples. At some cases, the identification of power harvesting responses can be obtained separately by analysing two different varying load resistances. For example, in Fig 3a, by choosing certain values of the tuning circuit parameters, the power amplitudes with the two peaks of resonance appear using optimal tuning inductance value where the maximum power amplitude can be achieved at the harvesting load resistance of $1.5 \text{ M}\Omega$. The two analytical techniques give good agreement. By scrutinizing Fig. 3b, the power harvesting responses using variable tuning circuit load resistances show the characteristic shifting responses based on the fixed harvesting load resistance of $1.5 \text{ M}\Omega$. Again, comparison between the two analytical techniques shows accurate results. Moreover, detail of the tuning behaviour can be seen in Fig. 4a, where the two peaks of resonance occur not only at the lower harvesting circuit load resistance around $80 \text{ k}\Omega$, but also at the higher harvesting circuit load resistance around $1.5 \text{ M}\Omega$. However, the two peaks of resonance at the harvesting circuit load resistance of $1.5 \text{ M}\Omega$ shows exactly the same response to that of Fig. 3a. Slightly different results can be seen in Fig. 4b, where shifting resonance frequency based on varying tuning circuit load resistance can be seen with the maximum amplitude from the chosen harvesting circuit load resistance of $1.5 \text{ M}\Omega$. The two figures show that the resonance can be widened by up to 7 Hz.

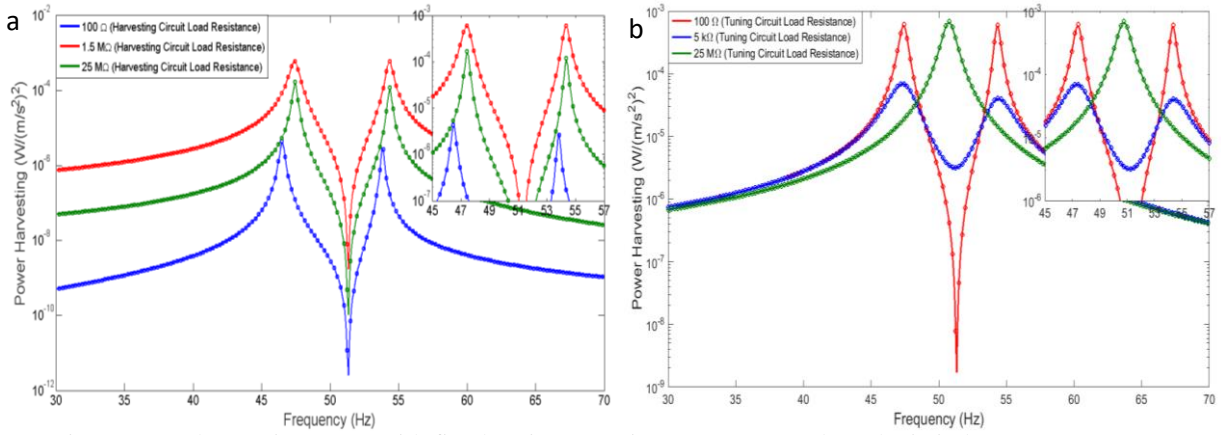


Fig.3. Power harvesting FRFs with fixed tuning capacitor $C = 20$ nF and synthetic inductance $L_s = 250.6$ H: a) variable harvesting load resistance with fixed tuning load resistances $R_l = 100 \Omega$ (solid line–closed form and circle–Ritz method), b) variable tuning load resistance with fixed harvesting load resistances $R_d = 1.5 \text{ M}\Omega$ (solid line–closed form and circle–Ritz method).

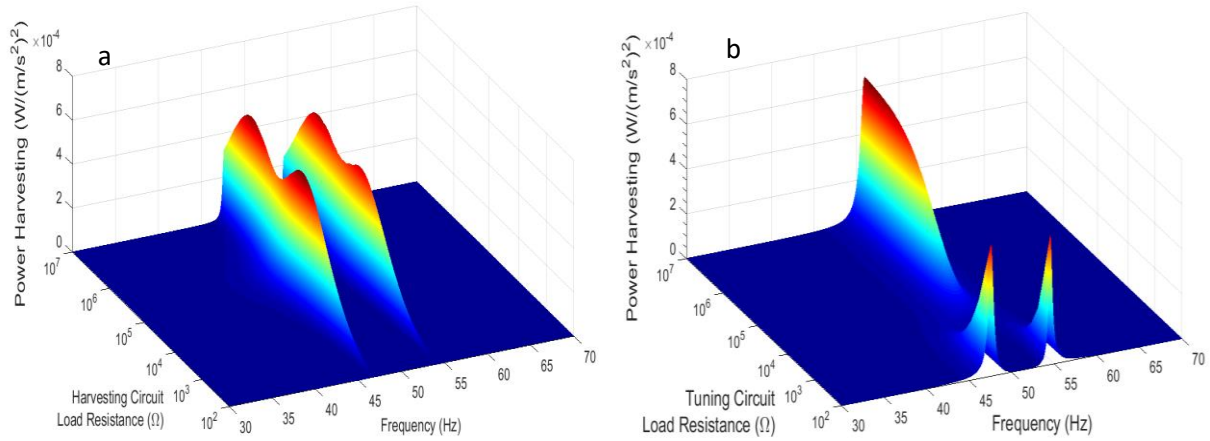
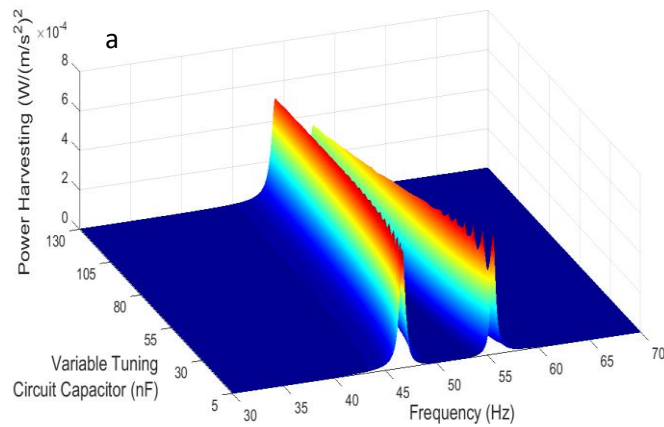


Fig.4. Power harvesting FRFs with fixed tuning capacitor 20 nF and synthetic inductance $L_s = 250.6$ H: a) variable harvesting load resistance with fixed tuning load resistance $R_l = 100 \Omega$, b) variable tuning load resistance with fixed harvesting load resistance $R_d = 1.5 \text{ M}\Omega$.



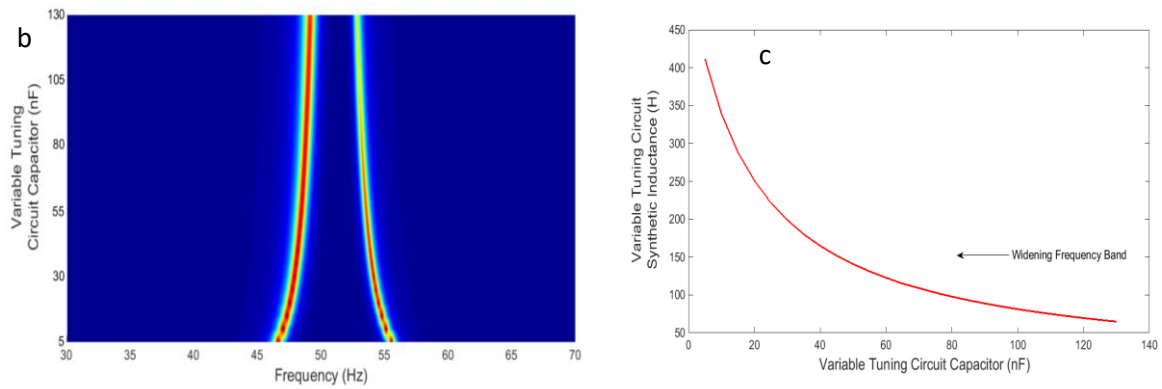


Fig.5. Power harvesting FRFs with fixed harvesting and tuning load resistances $R_d=1.5\text{ M}\Omega$ and $R_l=100\ \Omega$ respectively: a) variable tuning capacitance corresponding with variable synthetic inductance, b) contour response of Fig. 5a, c) relation of variable tuning capacitance and synthetic inductance being used in Fig.5a.

In Fig. 5a, the tuning power FRFs can also be set using different parametric circuit techniques. It is clearly seen from Fig. 5b that the bandwidth of the two peaks of resonance gradually increases with decreasing variable tuning capacitance or increasing variable inductance. Note that Fig. 5c can be used for identifying the inductance value using $L_s = P_C / \omega_r^2$. For example, the capacitance can be tuned to be a lower value resulting in larger inductance so as to widen the frequency band. For the higher inductance, the bandwidth of the two peaks of resonance seems to be more pronounced. The benefit is that the tuning level obtained can reach a maximum of 7 Hz using a tuning capacitance of 20 nF and even higher up to 10 Hz if the tuning capacitance of 5 nF was chosen as shown in Fig. 5b.

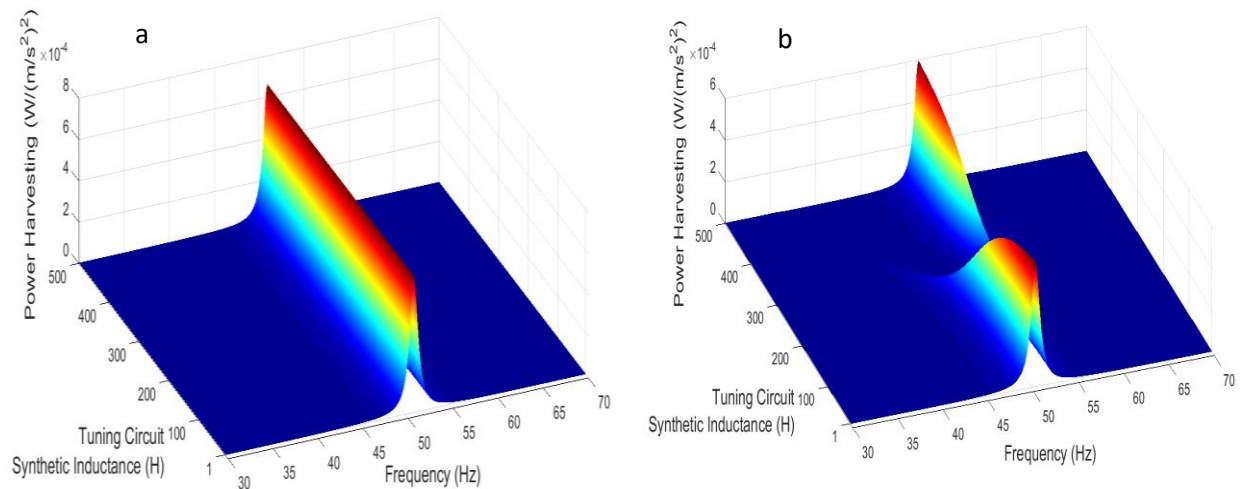


Fig.6. Power harvesting FRFs based on variable synthetic inductance with fixed tuning capacitance $C = 20\text{ nF}$ and harvesting load resistance $R_d = 1.5\text{ M}\Omega$: a) fixed tuning load resistance $R_l = 25\text{ M}\Omega$, b) fixed tuning load resistance $R_l = 5\text{ k}\Omega$.

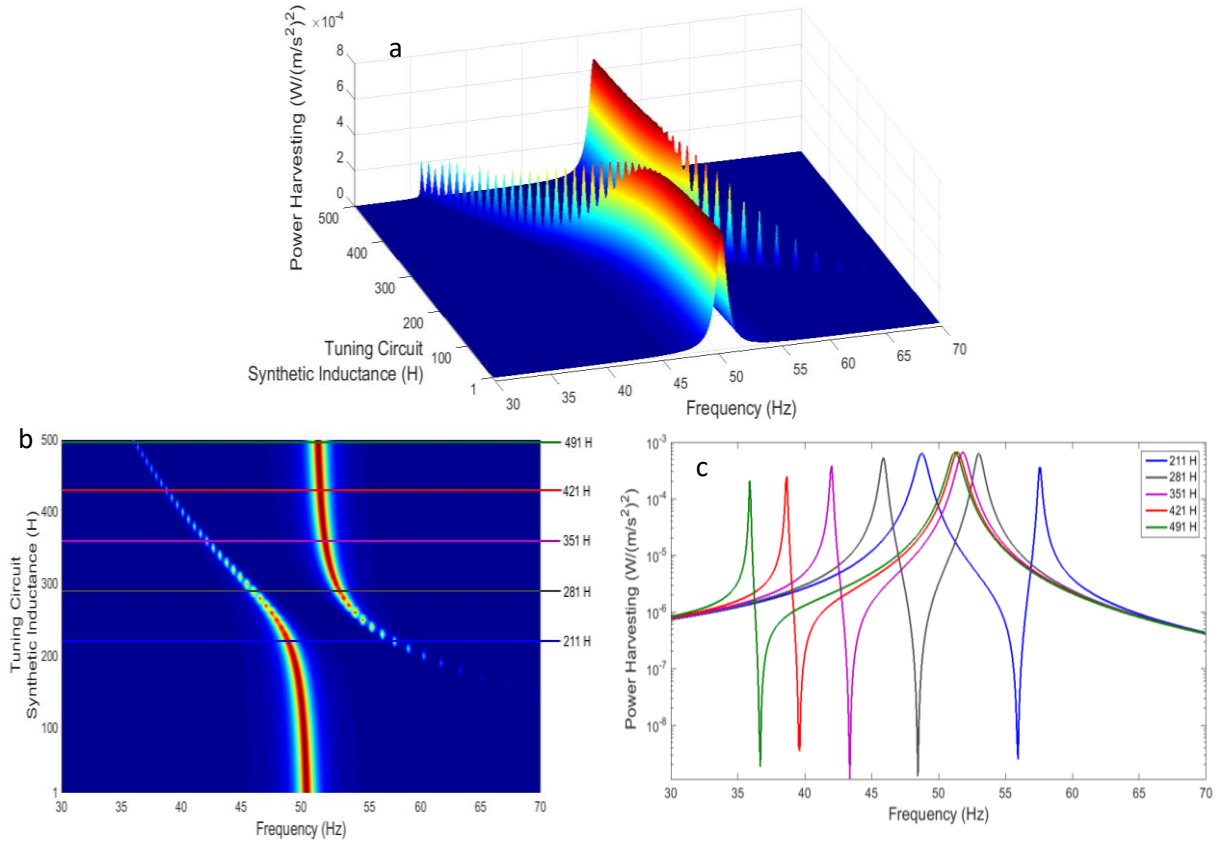


Fig. 7. Power harvesting FRFs with fixed tuning capacitance $C = 20$ nF and fixed harvesting and tuning load resistances $R_d = 1.5$ M Ω and $R_l = 100$ Ω respectively: a) variable synthetic inductance, b) contour response of Fig. 7a, c) snapshot at particular synthetic inductance values (slightly away from optimal inductance)

Unlike the tuning configuration of Fig. 5, Fig. 6a shows that the system power harvesting response remains constant with high amplitude. However, corresponding with the result shown in Fig. 6b, the power harvesting FRF begins to shift for the particular range of inductance. This occurs because the inductance value is exactly the same value as being used for the analysis in Fig. 3.

Moreover, Fig. 7a shows wider tuning system response compared with other previous case studies. For particular values of the fixed tuning and harvesting circuit load resistances, the shift of power harvesting frequency band with two peaks appears to be more pronounced for certain variable inductance values, even away from the optimal synthetic inductance ($L_s = 250.6$ H). It is clearly seen that the parameter tuning circuit for this case study show the most feasible and complementary guideline to simultaneously modify the power harvesting system responses. Figs. 7b and 7c clearly illustrate that the resonance frequency tuning can exceed 20 Hz as long as the tuning and harvesting circuit load resistances and tuning capacitance are chosen correctly.

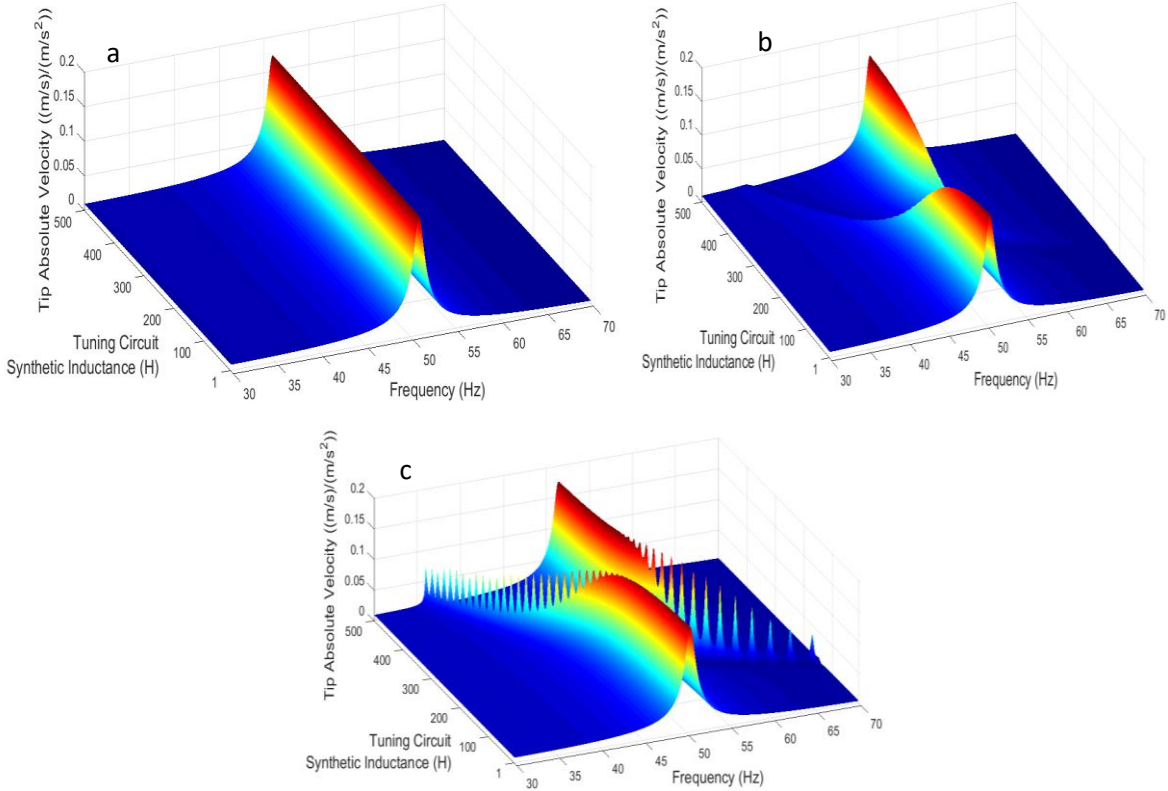


Fig.8. Tip absolute velocity FRFs based on variable synthetic inductance with fixed tuning capacitance $C = 20$ nF and harvesting load resistance $R_d = 1.5$ M Ω : a) fixed tuning load resistance $R_l = 25$ M Ω , b) fixed tuning load resistance $R_l = 5$ k Ω , c) fixed tuning load resistance $R_l = 100$ Ω .

As shown in Figs. 8a-8c, the three figures show different trend because certain harvesting and tuning circuit load resistance values cannot significantly affect the shift of velocity resonance frequency using certain tuning inductance values. This was aimed to explore how the tuning and harvesting circuit parameters affect each other in the self-adaptive response system. Furthermore, the system response as shown in Fig. 8c provides example of widening frequency band with the given multiple peaks of amplitude.

For DC harvesting electrical outputs, the voltage waveforms through the rectifier and capacitor can be seen in Figs. 9a and 10a with different operating tuning circuit capacitance values. The DC waveform behaviour as shown in Fig. 9a indicates a phenomenon of initial beat waveform due to the similar frequencies from the mechanical smart structure system and tuning circuit. However, this only occurs during the first 3 seconds and after that it is a constant time waveform with dramatic reduction of voltage. For this case, it is clearly seen that the power harvesting using optimal synthetic inductance may not be effective due to having a very low power amplitude range where it is only applicable for vibration suppression. As mentioned previously, the paper is aimed to find the most feasible tuning power harvesting systems where a few cases of ineffective tuning parameters are also presented for understanding the whole scenario of tuning effect in relation to the power harvesting scheme. In Fig. 9c, the DC power harvesting across load resistance also gives low amplitude. Two Hilbert envelopes of the initial beat signals for tip absolute velocity occur at the first two seconds as shown in Fig. 9d.

Detail of mathematical analysis of the Hilbert envelope reduced from Hilbert transform can be found in [62] where signal pattern detection of velocity time waveform can be seen clearly from the peak-to-peak amplitude. In Figs. 10a-10d, the DC voltage, capacitive DC current, DC power across load resistance and velocity signals tend to be constant after 1.5 seconds as being away from the beating frequency since the tuning circuit resonance is not similar with the smart structure system due to changing the value of the tuning circuit capacitance. Adding the smoothing capacitor onto the harvesting circuit clearly gives reduction of the ripple voltage as shown in red colour. As a result, the charging process through the capacitor at certain times only occurs for the ripple process each time the diodes conduct to capture the process of AC-DC current as shown in Fig. 10b. Once the capacitor discharges, no current will flow. In Fig. 10d, Hilbert envelope has also been detected from the velocity time waveform signal giving the accurate direct pattern of the mobility of the signal itself.

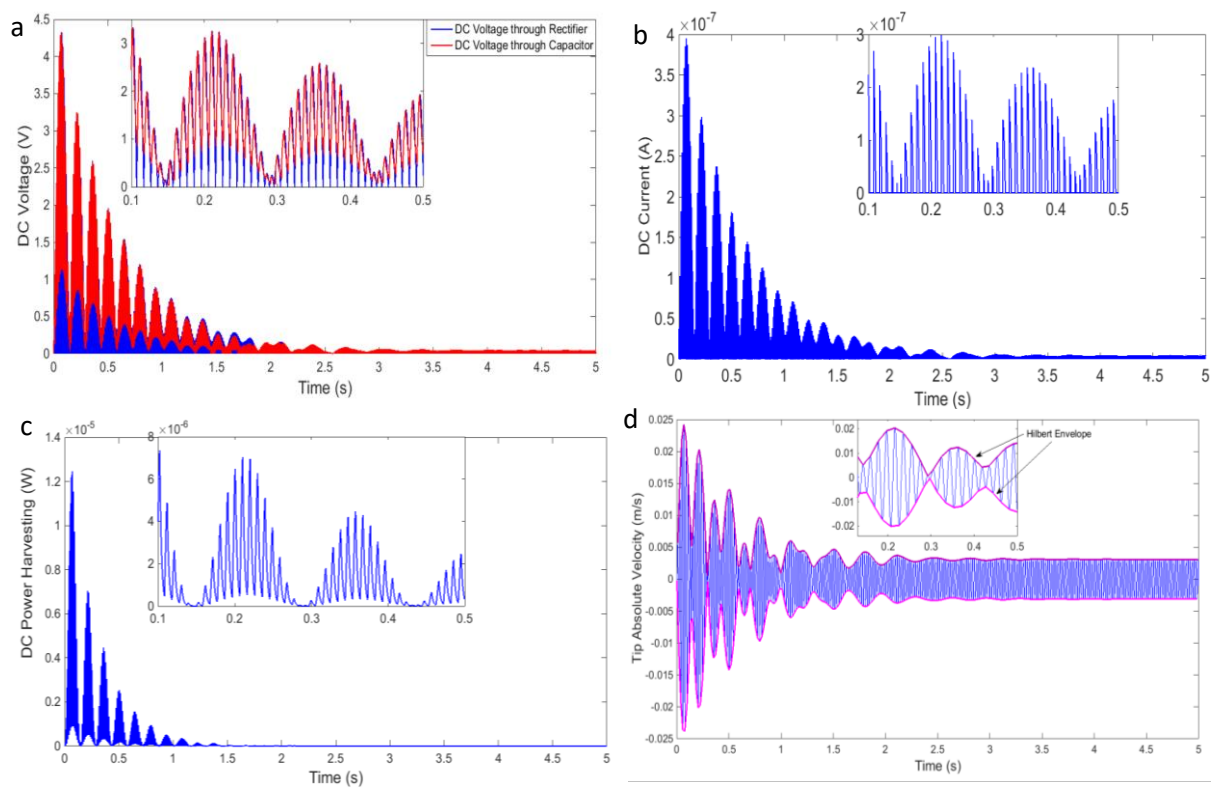


Fig. 9. Time waveform signal with initial beating phenomenon based on tuning capacitance $C = 20$ nF with synthetic inductance 250.6 H, harvesting capacitance $C_d = 0.3$ nF and harvesting and tuning load resistances $R_d = 1.5$ M Ω and $R_l = 100$ Ω : a) DC Voltage, b) DC capacitor current, c) DC power harvesting across load resistance, d) tip absolute velocity.

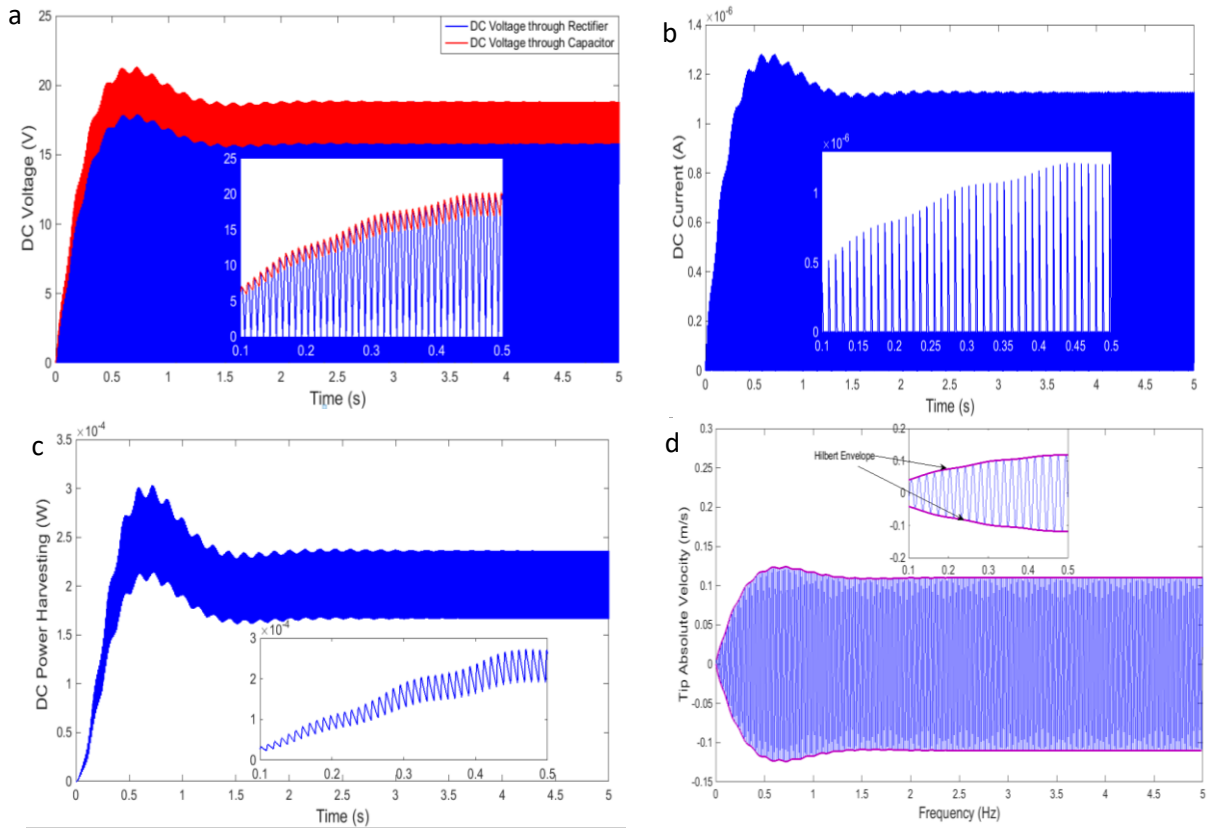


Fig. 10. Time waveform signal based on tuning capacitance $C = 30$ nF with synthetic inductance 250.6 H, harvesting capacitance 0.3 nF and harvesting and tuning load resistances $R_d=1.5$ M Ω and $R_l=100$ Ω :
a) DC Voltage, b) DC capacitor current, c) DC power harvesting across load, d) tip absolute velocity.

As shown in Fig. 11, increasing the broadband power harvesting across the load resistance can be identified by altering the tuning circuit inductance values (slightly away from optimal inductance value or away from the beat frequency signal). Overall, the power harvesting provides better tuning with higher amplitude. Moreover, the signal with the inductance of 421 H seems to be the most feasible tuning response giving higher amplitude and wider tuning frequency compared with other inductances. By viewing Fig. 12, the power harvesting across load resistance using tuning inductance of 421 H with tuning circuit capacitance of 20 nF also gives the highest time waveform amplitude. It is clearly seen that the tuning circuit capacitance also provides major effect to increase or decrease power harvesting amplitude.

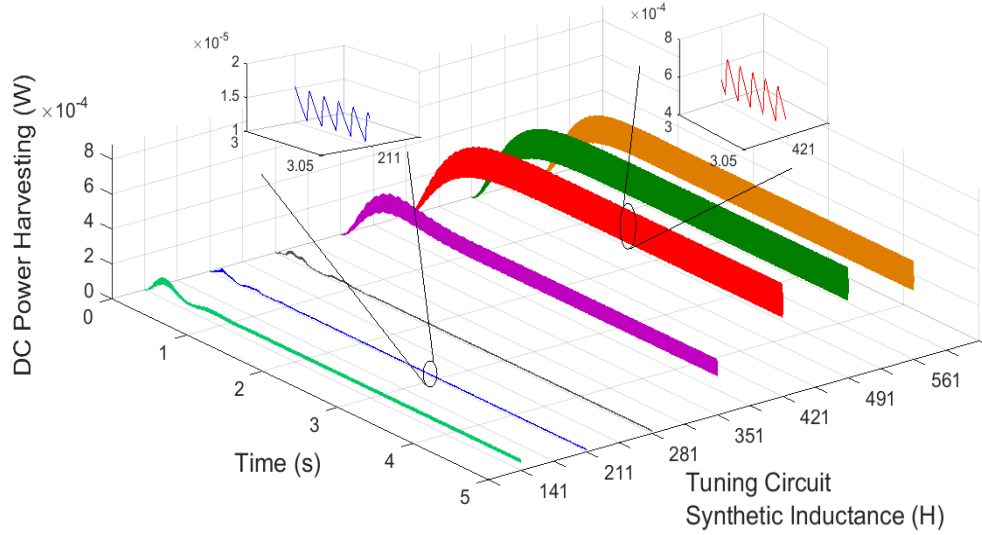


Fig. 11. Time waveform power harvesting based on variable synthetic inductance with harvesting and tuning capacitances $C_d = 0.3 \text{ nF}$ and $C = 20 \text{ nF}$, and harvesting and tuning load resistances $R_d = 1.5 \text{ M}\Omega$ and $R_l = 100 \Omega$.

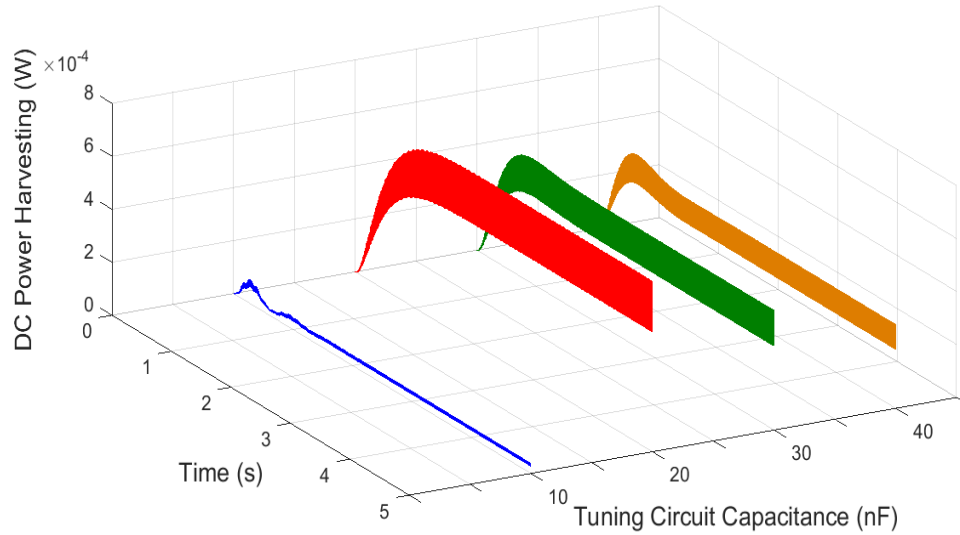


Fig. 12. Time waveform power harvesting based on variable tuning inductance with synthetic inductance $L_s = 421 \text{ H}$, harvesting capacitance $C_d = 0.3 \text{ nF}$ and harvesting and tuning load resistances $R_d = 1.5 \text{ M}\Omega$ and $R_l = 100 \Omega$.

The DC power harvesting waveform across load resistance as shown in Fig. 13 increases with increasing harvesting load resistance until reaching the maximum amplitude and then gradually decreases when reaching the open circuit load resistance. Note that the amount of ripple voltage reduces with increasing harvesting load resistance where the time of the capacitor to discharge decreases. This will give benefit for faster charging of the capacitor in many electronic applications. At this case, the capacitor in parallel with load resistance can provide a basic example of reducing the DC voltage ripple.

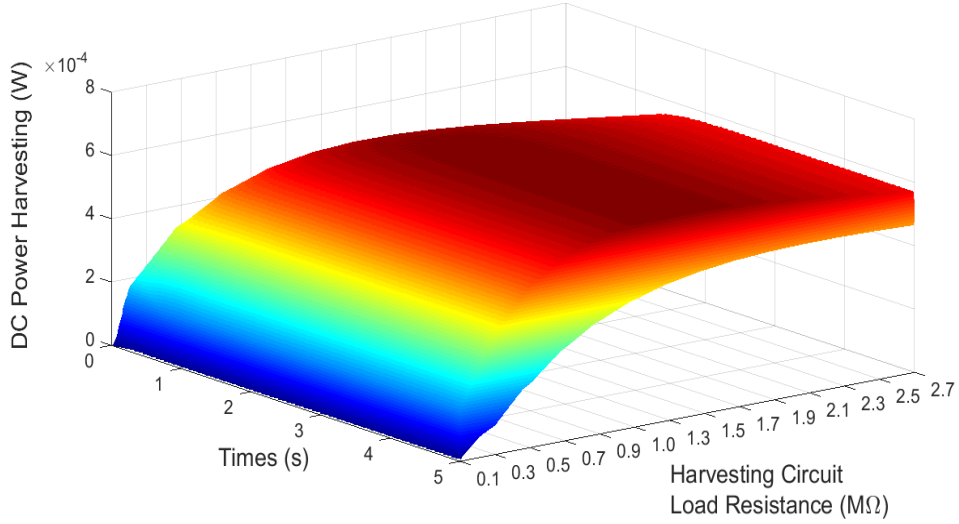


Fig. 13. Time waveform power harvesting based on variable harvesting load resistance with synthetic inductance $L_s = 421$ H, harvesting and tuning capacitances $C_d = 0.3$ nF and $C = 20$ nF, and tuning load resistance $R_l = 100$ Ω .

6. Conclusion

This paper has presented parametric case studies of the feasibility of tuning the piezoelectric power harvesters with the tip mass offset. Novel analytical techniques developed from the extended Hamiltonian principle have been derived using the dynamical closed-form boundary value method and the weak form analytical approach. Much attention for derivations has been given to the new normalised-three coupled electromechanical shunted piezoelectric power harvesting equations for formulating the complete forms of the new electromechanical multi-mode FRFs. Example of the validations between two analytical methods has also been shown, giving good agreement. Moreover, the combination of the shunt circuit control and power harvesting system has been explored to find the most feasible self-adaptive tuning harvesting response capabilities not only in the frequency response but also in the time waveform response.

The technical findings can be concluded as follows:

1. It is essential to identify the increasing power amplitudes and their tuning frequency using variable load resistance of the harvesting and tuning circuits with fixed tuning inductance and capacitor (optimal tuning circuit) before exploring other tuning parameters. It was found that the power FRFs increase followed by widening frequency bandwidth up to 7 Hz with certain harvesting and tuning circuit load resistance values. Examples can be seen in Figs. 3 and 4. However, point 5 below also discusses their relations with the time waveform giving a reduction of power amplitude which is not effective for the power harvesting scheme.
2. Shift of power harvesting resonance can be achieved over a moderate larger range using variable tuning capacitance corresponding with the synthetic inductance representing the optimal tuning circuit. The larger frequency shift can extend up to 10 Hz. Examples can be seen in Fig. 5. This

case provides a guideline to identify the frequency tuning behaviour. However, the discussion in point 5 below shows that the example of choosing the optimal tuning circuit may not be effective for power harvesting systems due to very low time waveform amplitude. Alternative solutions for the most feasible and effective tuning power harvesting scheme is further discussed in points 4 and 6 below.

3. Shunt circuit control can also provide benefit for the use of sensitive and automatic frequency tuning responses from lower to moderate larger ranges if it is difficult to find a precise resonance match from the mechanical tuning system of the smart structure.
4. Wider tuned power harvesting frequency band can be achieved using variable tuning inductance (away slightly from its optimal value) with certain values of the fixed tuning and harvesting circuit load resistances and fixed tuning capacitance. This case study provides examples of the most feasible tuning systems compared with other parametric studies. Examples can be seen in Fig. 7. It is important to note that this case study was obtained once the previous essential parametric case studies have been explored so as to further use the best values of harvesting and tuning load resistances, inductance and capacitance for identifying the maximum amplitude and widened frequency range.
5. Using the optimal tuning circuit, the initial beating phenomenon of the time waveform DC power occurs followed by a dramatic reduction of amplitude. After a beating signal of less than a few seconds, the waveform amplitude seems to remain constant with very low value. Examples of this can be seen in Fig. 9. In relation with Fig. 3 with the same tuning circuit parameter, the power harvesting FRFs using the optimal circuit provides wider bandwidth, but in the time waveform the power decreases dramatically showing initial beating phenomenon. At this case the optimal circuit system may not be effective due to having very low amplitude, but is applicable for vibration suppression as many previous publications in the shunt control system have shown.
6. Time waveform DC power harvesting using particular synthetic inductances being away from its optimal value provides effective ways to give the fluctuated amplitude in the time domain as being away from a beating frequency signal (away from an optimal synthetic inductance or optimal tuning circuit). Increasing power amplitudes are also affected by the use of certain values of the tuning circuit capacitance and harvesting load resistance. Examples of this can be seen in Figs.11-13 with very high power amplitudes. Incorporating Fig. 7, the widening power harvesting FRFs can be achieved more than 20 Hz, giving the most feasible and effective tuning parameters in the application of the power harvesting system.

Overall, the frequency response and time waveform power harvesting using the effect of the tuning circuit parameters are important aspects to be explored since the parametric case studies can provide the guideline to identify the most feasible tuning system in terms of the widening frequency band and

its amplitude. Also, the multiple shunt circuit networks for future work can also give further benefit for multiple wider tuning systems.

Appendix A. Modified Elastic Constant and Piezoelectric Constant

The modified elastic constant and piezoelectric constant for tuning and harvesting piezoelectric layers can be formulated, respectively as,

$$\bar{c}_D^{(1)} = \bar{c}_{11}^{(1,E)} + e_{31}^{(1)^2} \varepsilon_{33}^{(1,S)^{-1}}, \quad g_{31}^{(1)} = \varepsilon_{33}^{(1,S)^{-1}} e_{31}^{(1)}, \quad (\text{A.1})$$

$$\bar{c}_D^{(3)} = \bar{c}_{11}^{(3,E)} + e_{31}^{(3)^2} \varepsilon_{33}^{(3,S)^{-1}}, \quad g_{31}^{(3)} = \varepsilon_{33}^{(3,S)^{-1}} e_{31}^{(3)}. \quad (\text{A.2})$$

Note that general parameter $\varepsilon_{33}^{(i,S)}$ for piezoelectric layers (superscript $i \in \{1,3\}$) indicates the permittivity at constant strain (superscript S) $\varepsilon_{33}^{(i,S)} = \varepsilon_{33}^{(i,T)} - e_{31} d_{31}^{(i)}$ or $\varepsilon_{33}^{(i,S)} = \varepsilon_{33}^{(i,T)} - d_{31}^2 c_{11}^{(i,E)}$ where $\varepsilon_{33}^{(i,T)}$ is the permittivity at constant stress (superscript T).

Appendix B. Stiffness Coefficients for the Smart Structure

The total transverse stiffness coefficient for triple layers can be formulated as,

$$C_t = \frac{1}{3} \left(\sum_{i=1}^m \bar{c}_D^{(i)} b^{(i)} \left(\sum_{j=i}^m h^{(j)} - z_n \right)^3 - \sum_{i=1}^{m-1} \bar{c}_D^{(i)} b^{(i)} \left(\sum_{j=i+1}^m h^{(j)} - z_n \right)^3 + \bar{c}_D^{(m)} b^{(m)} z_n^3 \right). \quad (\text{B.1})$$

Note that $\bar{c}_D^{(2)} = \bar{c}_{11}^{(2)}$ is the non-piezoelectric material and neutral axis z_n can be seen in Appendix C.

Parameter b is the width of the interlayer and term m is number of layers.

Appendix C. Determining the Neutral Axis of the Smart Structure

In Fig. 1, the location of the asymmetric neutral axis measured from the x -axis to the top surface of the piezoelectric layer can be determined to give,

$$z_n = \frac{\sum_{i=1}^m \bar{c}_D^{(i)} h^{(i)^2} b^{(i)} + 2 \sum_{i=1}^{m-1} \bar{c}_D^{(i)} h^{(i)} b^{(i)} \sum_{j=i+1}^m h^{(j)}}{2 \sum_{i=1}^m \bar{c}_D^{(i)} h^{(i)} b^{(i)}}. \quad (\text{C.1})$$

Appendix D. Modified Transverse Piezoelectric Coupling Coefficient and Modified Piezoelectric Internal Capacitance

Modified transverse piezoelectric coupling in the tuning and harvesting piezoelectric layers can be formulated, respectively as,

$$\eta^{(1)} = \frac{g_{31}^{(1)} \left(h^{(1)2} + 2h^{(1)}h^{(3)} + 2h^{(2)}h^{(1)} - 2z_n h^{(1)2} \right)}{2L},$$

$$\eta^{(3)} = \frac{g_{31}^{(3)} \left(2z_n h^{(3)} - h^{(3)2} \right)}{2L}. \quad (\text{D.1})$$

The modified internal capacitances in the tuning and harvesting piezoelectric layers can be stated, respectively as,

$$C_v^{(1)} = \frac{\varepsilon_{33}^S b^{(1)} L}{h^{(1)}}, \quad C_v^{(3)} = \frac{\varepsilon_{33}^S b^{(3)} L}{h^{(3)}}. \quad (\text{D.2})$$

Appendix E. Mode shapes of the Triple Layer Beam with Proof Mass Offset

The mode shape of transverse bending can be formulated as,

$$W_r(x) = a_{1r} \left(\cos(\alpha x) - \cosh(\alpha x) + \frac{A_{21}}{A_{22}} (\sin(\alpha x) - \sinh(\alpha x)) \right). \quad (\text{E.1})$$

where: $A_{21} = (\sin(\alpha L) - \sinh(\alpha L)) + \frac{I_0^{tip} \alpha}{I_0} (\cos(\alpha L) - \cosh(\alpha L)) - \frac{x_c I_0^{tip} \alpha^2}{I_0} (\sin(\alpha L) + \sinh(\alpha L))$,

$$A_{22} = (\cos(\alpha L) + \cosh(\alpha L)) - \frac{I_0^{tip} \alpha}{I_0} (\sin(\alpha L) - \sinh(\alpha L)) - \frac{x_c I_0^{tip} \alpha^2}{I_0} (\cos(\alpha L) - \cosh(\alpha L)). \quad (\text{E.2})$$

Since Eq. (E1) contains variable a_{1r} as the transverse amplitude constant, the normalised mode shape can be formulated as,

$$\hat{W}_r(x) = \frac{W_r(x)}{\left(\int_0^L I_0 W_r(x)^2 dx + I_0^{tip} W_r(L)^2 + 2x_c I_0^{tip} W_r(L) \frac{dW_r}{dx}(L) + I_2^{tip} \left(\frac{dW_r}{dx}(L) \right)^2 \right)^{1/2}}, r=1,2,\dots, m. \quad (\text{E.3})$$

References

- [1] Roundy S and Wright P K 2004 A piezoelectric vibration based generator for wireless electronics *Smart Mater. Struct.* **18** 1131–1142
- [2] Takeda H, Mihara K, Yoshimura T, Hoshina T and Tsurumi T 2011 Effect of material constants on power output in piezoelectric vibration-based generators *IEEE Trans. Ultrason. Ferroelectr. Freq. Control* **58** 1852-1859
- [3] Shu Y C and Lien I C 2006 Analysis of power output for piezoelectric energy harvesting systems *Smart Mater. Struct.* **15** 1499–512
- [4] Guyomar D, Badel A, Lefeuvre E and Richard C 2005 Toward energy harvesting using active materials and conversion improvement by nonlinear processing *IEEE Trans. Ultrason. Ferroelectr. Freq. Control* **52** 584–595
- [5] Shu Y C, Lien I C and Wu W J 2007 An improved analysis of the SSHI interface in piezoelectric

energy harvesting *Smart Mater. Struct.* **16** 2253–2264

- [6] Tang L and Yang Y 2011 Analysis of synchronized charge extraction for piezoelectric energy Harvesting *Smart Mater. Struct.* **20** 085022
- [7] Liao Y and Sodano H 2008 Model of a single mode energy harvester and properties for optimal power generation *Smart Mater. Struct.* **17** 065026
- [8] Liao Y and Sodano H 2010 Modeling and comparison of bimorph power harvesters with piezoelectric elements connected in parallel and series *J. Intell. Mater. Syst. Struct.* **21** 149–59
- [9] Goldschmidtboeing F and Woias P 2008 Characterization of different beam shapes for piezoelectric energy harvesting *J. Micromech. Microeng.* **18** 104013
- [10] Kim M, Hoegen M, Dugundji J and Wardle B L 2010 Modeling and experimental verification of proof mass effects on vibration energy harvester performance *Smart Mater. Struct.* **19** 045023
- [11] Erturk A and Inman D J 2009 An experimentally validated bimorph cantilever model for piezoelectric energy harvesting from base excitations *Smart Mater. Struct.* **18** 025009
- [12] Wang H and Meng Q 2013 Analytical modeling and experimental verification of vibration-based piezoelectric bimorph beam with a tip-mass for power harvesting *Mech. Syst. Signal Proc.* **36** 193–209.
- [13] Lumentut M F and Howard I M 2013 Analytical and experimental comparisons of electromechanical vibration response of a piezoelectric bimorph beam for power harvesting *Mech. Syst. Signal Proc.* **36** 66–86
- [14] Lumentut M F and Howard I M 2011 Analytical modeling of self-powered electromechanical piezoelectric bimorph beams with multidirectional excitation *Int. J. Smart Nano Mater.* **2** 134–175
- [15] Erturk A 2012 Assumed-modes modeling of piezoelectric energy harvesters: Euler–Bernoulli, Rayleigh, and Timoshenko models with axial deformations *Comp. Struct.* **106-107** 214–227
- [16] Wickenheiser A M 2013 Eigensolution of piezoelectric energy harvesters with geometric discontinuities: Analytical modelling and validation *J. Intel. Mater. Syst. Struct.* **24**, 729–744
- [17] Dalzell P and Bonello P 2012 Analysis of an energy harvesting piezoelectric beam with energy storage circuit *Smart Mater. Struct.* **21**105029
- [18] Zhu M, Worthington E and Njuguna J 2009 Analyses of power output of piezoelectric energy-harvesting devices directly connected to a load resistor using a coupled piezoelectric-circuit finite element method *IEEE Trans. Ultrason. Ferroelectr. Freq. Control* **56** 1309–1318
- [19] Elvin N G and Elvin A A 2009 Coupled finite element-circuit simulation model for analyzing piezoelectric energy generators *J. Intel. Mater. Syst. Struct.* **20** 587-595
- [20] Yang Y and Tang L 2009 Equivalent circuit modeling of piezoelectric energy harvesters *J. Intell. Mater. Syst. Struct.* **20** 2223-2235

- [21] DeMarqui Jr. C, Erturk A and Inman D J 2009 An electromechanical finite element model for piezoelectric energy harvester plates *J. Sound Vib.* **327** 9–25
- [22] Lumentut M F and Howard I M 2014 Electromechanical finite element modelling for dynamic analysis of a cantilevered piezoelectric energy harvester with tip mass offset under base excitations *Smart Mater. Struct.* **23** 095037
- [23] Wu X, Lin J, Kato S, Zhang K, Ren T, Liu L 2008 A frequency adjustable vibration energy harvester. In: *Proceedings of PowerMEMS*, 245–248
- [24] Erturk A, Renno J M, Inman D J 2009 Modeling of piezoelectric energy harvesting from an L-shaped beam-mass structure with an application to UAVs *J. Intell. Mater. Syst Struct* **20** 529–544
- [25] Karami, A and Inman D J 2011 Electromechanical modeling of the low frequency zigzag micro energy harvester, *J. Intell. Mat. Syst. Struct.*, **22**(3), 271-282
- [26] Wu H, Tang L, Yang Y and Soh C K 2012 A novel two-degrees-of-freedom piezoelectric energy harvester *J. Intell. Mater. Syst. Struct.* **24** 357–368
- [27] Berdy D F, Srisungsitthisunti P, Jung B, Xu X, Rhoads J F and Peroulis D 2012 Low-Frequency Meandering Piezoelectric Vibration Energy Harvester *IEEE Trans. Ultrason. Ferroelectr. Freq. Control* **59** 846-858
- [28] Xue H, Hu Y and Wang Q.-M 2008 Broadband piezoelectric energy harvesting devices using multiple bimorphs with different operating frequencies *IEEE Trans. Ultrason. Ferroelectr. Freq. Control* **55** 2104-2108
- [29] Lumentut M F, Francis L A and Howard I M 2012 Analytical techniques for broadband multielectromechanical piezoelectric bimorph beams with multifrequency power harvesting *IEEE Trans. Ultrason. Ferroelectr. Freq. Control* **59** 1555-68
- [30] Zhang H and Afzalul K 2014 Design and analysis of a connected broadband multi-piezoelectric-bimorph-beam energy harvester, *IEEE Trans. Ultrason. Ferroelectr. Freq. Control* **61** 1016-1023
- [31] Lien I C and Shu Y C 2012 Array of piezoelectric energy harvesting by the equivalent impedance approach *Smart Mater. Struct.* **21** 082001
- [32] Lien I C, Shu Y C, Wu W J and Lin H C 2010 Revisit of series-SSHI with comparisons to other interfacing circuits in piezoelectric energy harvesting *Smart Mater. Struct* **19** 125009
- [33] Lin H C, Wu P H, Lien I C, and Shu Y C 2013 Analysis of an array of piezoelectric energy harvesters connected in series *Smart Mater. Struct* **22** 094026
- [34] Roundy S and Zhang Y 2005 Toward self-tuning adaptive vibration based micro-generators. *Proc. SPIE* 5649:373–384
- [35] Lallart M, Anton S R and Inman D J 2010 Frequency self-tuning scheme for broadband vibration energy harvesting *J Intell Mater Syst Struct* **21** 897–906
- [36] Wu W-J, Chen Y-Y, Lee B-S, He J-J and Peng Y-T 2006 Tunable resonant frequency power Harvesting devices *Proc. SPIE* **6169** 55–62

- [37] Charnegie D 2007 Frequency tuning concepts for piezoelectric cantilever beams and plates for energy harvesting *MSc Dissertation* School of Engineering, University of Pittsburgh, USA.
- [38] Forward R L 1979 Electronic damping of vibrations in optical structures *Appl. Opt.* **18** 690–697
- [39] Hagood N W, Chung W H and Flowtow A v 1990 Modelling of piezoelectric actuator dynamics for active structural control *J Intell Mater Syst Struct* **1** 327-354
- [40] Caruso G 2001 A critical analysis of electric shunt circuits employed in piezoelectric passive vibration damping *Smart Mater. Struct.* **10** 1059–68
- [41] Niederberger D and Morari M 2006 An autonomous shunt circuit for vibration damping *Smart Mater. Struct.* **15** 359–364
- [42] Thomas O, Ducarne J and De`u J-F 2012 Performance of piezoelectric shunts for vibration Reduction *Smart Mater. Struct.* **21** 015008
- [43] Vasques C M A 2012 Improved passive shunt vibration control of smart piezo-elastic beams using modal piezoelectric transducers with shaped electrodes *Smart Mater. Struct.* **21** 125003
- [44] Moheimani S O R and Fleming A J 2006 Piezoelectric Transducers for Vibration Control and Damping (Springer London)
- [45] Riordan R H S 1967 Simulated inductors using differential amplifiers *Electron. Lett.* **3** 50-51
- [46] Antoniou A 1967 Gytrators using operational amplifiers *Electron. Lett.* **3** 350-352
- [47] Tellegen, B D H 1948 The gyrator, a new electric network element, *Philips Res. Rep.* **3** 81-101
- [48] Hollkamp J J 1994 Multimode Passive Vibration Suppression with Piezoeleircic Materials and Resonant Shunts *J. Intell. Mater. Syst. Struct.* **5** 45-57
- [49] Behrens S, Fleming A J and Moheimani S O R 2003 A broadband controller for shunt piezoelectric damping of structural vibration *Smart Mater. Struct.* **12** 36–48
- [50] Maurini C, dell’Isola F and Del Vescovo D 2004 Comparison of piezoelectronic networks acting as distributed vibration absorbers *Mech. Syst.Signal Proc.* **18** 1243–1271
- [51] Niederberger D, Fleming A, Moheimani S O R and Morari M 2004 Adaptive multi-mode resonant piezoelectric shunt damping *Smart Mater. Struct.* **13** 1025–1035
- [52] Moheimani S O R 2003 A survey of recent innovations in vibration damping and control using shunted piezoelectric transducers, *IEEE Trans. Control Syst. Tech.* **11** 482–494
- [53] Fleming A J, Behrens S and Moheimani S O R 2002 Optimization and implementation of multi-mode piezoelectric shunt damping systems *IEEE/ASME Trans. Mechatronics* **7** 87–94
- [54] Moheimani S O R 2004 Multimode Piezoelectric Shunt Damping With a Highly Resonant Impedance *IEEE Trans.Control Syst. Tech.* **12** 484-491
- [55] Giorgio I, Culla A and Del Vescovo D 2009 Multimode vibration control using several piezoelectric transducers shunted with a multiterminal network *Arch. App. Mech.* **79** 859-879
- [56] Tiersten H F 1969 Linear piezoelectric plate vibrations (Plenum Press)

- [57] Nye J F 1984 Physical properties of crystals: their representation by tensors and matrices, (Oxford, England: Clarendon Press)
- [58] Ikeda T 1990 Fundamentals of piezoelectricity (New York: Oxford University Press)
- [59] Standards Committee of the IEEE Ultrasonics, Ferroelectrics, and Frequency Control Society 1987 *IEEE standard on piezoelectricity* (New York: IEEE)
- [60] Ritz W 1909 Über eine neue Methode zur Lösung gewisser Variationsprobleme der mathematischen Physik *Journal für die Reine und Angewandte Mathematik* **135** 1–61.
- [61] Courant R and Hilbert D 1953-1962 Methoden der mathematischen physik / English Ed.: Methods of mathematical physics (New York : Interscience Publishers)
- [62] Feldman M 2011 Hilbert transform in vibration analysis, *Mech. Syst. Signal Proc.* **25** 735–802